

NEARLY SELF-SIMILAR BLOWUP OF GENERALIZED AXISYMMETRIC NAVIER–STOKES AND BOUSSINESQ EQUATIONS

THOMAS Y. HOU

DEDICATED TO RUSSEL CAFLISCH ON THE OCCASION OF HIS 70TH BIRTHDAY

ABSTRACT. We perform numerical investigation of nearly self-similar blowup of generalized axisymmetric Navier–Stokes equations and Boussinesq system with a time-dependent fractional dimension. The dynamic change of the space dimension is proportional to the ratio $R(t)/Z(t)$, where $(R(t), Z(t))$ is the position at which the vorticity achieves its global maximum. This choice of space dimension is to ensure that the advection along the r direction has the same scaling as that along the z direction, thus preventing formation of two-scale solution structure. For the generalized axisymmetric Navier–Stokes equations with solution dependent viscosity, we show that the solution develops a self-similar blowup with dimension equal to 3.188 and the self-similar profile satisfies the axisymmetric Navier–Stokes equations with constant viscosity. We also study the nearly self-similar blowup of the axisymmetric Boussinesq system with constant viscosity. The generalized axisymmetric Boussinesq system preserves almost all the known properties of the 3D Navier–Stokes equations except for the conservation of angular momentum. We present convincing numerical evidence that the generalized axisymmetric Boussinesq system develops a stable nearly self-similar blowup solution with maximum vorticity increased by $O(10^{30})$.

I. INTRODUCTION

The question of global well-posedness of the 3D incompressible Euler and Navier–Stokes equations is one of the most important fundamental questions in nonlinear partial differential equations [31]. The main difficulty is due to the presence of vortex stretching. There has been some recent exciting developments for the singularity formation of the 3D incompressible Euler equations in the presence of boundary or with C^α initial vorticity, see e.g. [26, 27, 14, 12, 28, 29, 11, 22, 21]. However, not much progress has been made for the 3D incompressible Navier–Stokes equations with smooth initial data in the interior domain. In two recent papers by the author [35, 36], we proposed a new blowup candidate for the axisymmetric Navier–Stokes equations that develop a tornado like traveling wave solution with maximum vorticity increased by a factor of 10^7 .

Inspired by the work [35, 36], we perform numerical study of finite time singularity of the generalized axisymmetric Navier–Stokes and Boussinesq equations. Let u^θ , ω^θ , and ψ^θ be the angular velocity, angular vorticity, and angular stream function, respectively. We define $u_1 = u^\theta/r$, $\omega_1 = \omega^\theta/r$ and $\psi_1 = \psi^\theta/r$. Denote by $\Gamma = ru^\theta$ as the total circulation. It is well known that the total circulation satisfies an important conservation property. In this paper, we propose the following generalized n -dimensional axisymmetric Navier–Stokes equations formulated in terms of $(\Gamma, \omega_1, \psi_1)$ as follows:

$$\Gamma_t + u^r \Gamma_r + u^z \Gamma_z = \nu \left(\Gamma_{rr} + \frac{(n-4)}{r} \Gamma_r + \frac{(6-2n)}{r^2} \Gamma + \Gamma_{zz} \right), \quad (\text{I.1a})$$

$$\omega_{1,t} + u^r \omega_{1,r} + u^z \omega_{1,z} = \left(\frac{\Gamma^2}{r^4} \right)_z - (n-3) \psi_{1,z} \omega_1 + \nu \left(\omega_{1,rr} + \frac{n}{r} \omega_{1,r} + \omega_{1,zz} \right), \quad (\text{I.1b})$$

$$-\left(\partial_r^2 + \frac{n}{r} \partial_r + \partial_z^2 \right) \psi_1 = \omega_1, \quad (\text{I.1c})$$

where $u^r = -(r^{n-2}\psi^\theta)_z/r^{n-2}$, $u^z = (r^{n-2}\psi^\theta)_r/r^{n-2}$ and n ($n \geq 2$ can be any positive real number) is the space dimension. When $n = 3$, we recover the 3D axisymmetric Navier–Stokes equations. This generalized version of the axisymmetric Navier–Stokes equations enjoys almost all the known properties of the 3D axisymmetric Navier–Stokes equations, including the conservation of the total circulation and the incompressibility condition $(r^{n-2}u^r)_r + (r^{n-2}u^z)_z = 0$. Moreover, we will show that the kinetic energy $\int (|u_1|^2 + |\nabla\psi_1|)r^n dr dz = \int |\mathbf{u}|^2 r^{n-2} dr dz$ is conserved for smooth solutions and a fixed n . To the best of our knowledge, all the known non-blowup criteria also apply to the generalized axisymmetric Navier–Stokes equations for a given constant dimension n .

1.1. Self-similar blowup of the generalized Navier–Stokes equations. We first investigate the nearly self-similar blowup of the generalized axisymmetric Navier–Stokes equations with smooth initial data and solution dependent viscosity. Denote by $(R(t), Z(t))$ the position where $u_1(t, r, z) = \Gamma/r^2$ achieves its global maximum. Our solution dependent viscosity is given by $\nu = \nu_0 \|u_1(t)\|_\infty Z(t)^2$ with $\nu_0 = 0.006$. Note that this solution dependent viscosity is scaling invariant. This choice of solution dependent viscosity is to enforce the balance between vortex stretching term and the diffusion term. We choose the space dimension n to be $n = 1 + 2R(t)/Z(t)$, which is also scaling invariant. This choice of the dimension is to balance the advection along the r and z directions since u^r scales like $(R(t)/Z(t))\psi$ while u^z scales like ψ . By choosing n to scale like $R(t)/Z(t)$, we ensure that u^r and u^z have the same scaling as $R(t)$ and $Z(t)$ approach to zero, which prevents formation of two-scale blowup.

Our study shows that the generalized Navier–Stokes equations with this solution dependent viscosity develop a nearly self-similar blowup solution of the form:

$$\begin{aligned}\psi_1(t, r, z) &= \frac{\lambda(t)}{(T-t)^{1/2}} \Psi_1 \left(t, \frac{r}{\lambda(t)\sqrt{(T-t)}}, \frac{z}{\lambda(t)\sqrt{(T-t)}} \right), \\ u_1(t, r, z) &= \frac{1}{(T-t)} V_1 \left(t, \frac{r}{\lambda(t)\sqrt{(T-t)}}, \frac{z}{\lambda(t)\sqrt{(T-t)}} \right), \\ \omega_1(t, r, z) &= \frac{1}{\lambda(t)(T-t)^{3/2}} \Omega_1 \left(t, \frac{r}{\lambda(t)\sqrt{(T-t)}}, \frac{z}{\lambda(t)\sqrt{(T-t)}} \right),\end{aligned}$$

where $\lambda(t) \approx (T-t)^{0.0233}$ and we normalize V_1 to satisfy $V_1(R(t), Z(t)) = 1$. If we denote $\lambda(t)\sqrt{(T-t)} \equiv (T-t)^{c_1}$, then we have $c_1 = 0.5233$ and $\nu = \nu_0 \|u_1\|_\infty Z(t)^2 = \nu_0 (T-t)^{2c_1-1}$ since $Z(t) = (T-t)^{c_1}$. We observe that the maximum vorticity has the same scaling as $\|u_1(t)\|_\infty$. This implies that $\|\omega(t)\|_\infty$ scales like $O((T-t)^{-1})$, which violates the Beale-Kato-Majda non-blowup criterion [1]. An interesting observation is that the self-similar profile (Ψ_1, V_1, Ω_1) satisfies the self-similar generalized Navier–Stokes equations with a constant viscosity ν_0 and dimension $n \approx 3.188$.

1.2. Generalized axisymmetric Boussinesq system. We also investigate a generalized axisymmetric Boussinesq system with two constant viscosity coefficients by treating $\Gamma = ru^\theta$ as density and removing the $(n-3)\psi_{1,z}\omega_1$ term from our generalized Navier–Stokes equations. The generalized Boussinesq system is transported by the axisymmetric velocity $\mathbf{u} = u^r e_r + u^z e_z$ with no swirl.

$$\Gamma_t + u^r \Gamma_r + u^z \Gamma_z = \nu_1 \left(\Gamma_{rr} + \frac{(n-4)}{r} \Gamma_r + \frac{(6-2n)}{r^2} \Gamma + \Gamma_{zz} \right), \quad (\text{I.2a})$$

$$\omega_{1,t} + u^r \omega_{1,r} + u^z \omega_{1,z} = \left(\frac{\Gamma^2}{r^4} \right)_z + \nu_2 \left(\omega_{1,rr} + \frac{n}{r} \omega_{1,r} + \omega_{1,zz} \right), \quad (\text{I.2b})$$

$$- \left(\partial_r^2 + \frac{n}{r} \partial_r + \partial_z^2 \right) \psi_1 = \omega_1, \quad (\text{I.2c})$$

where $u^r = -(r^{m-2}\psi^\theta)_z/r^{m-2}$, $u^z = (r^{m-2}\psi^\theta)_r/r^{m-2}$ and $m = (n+3)/2$. We show that for $n < 7$, the generalized energy $\int (|u^\theta|^2 + \frac{(7-n)}{4}(|u^r|^2 + |u^z|^2)r^{n-2})drdz$ is conserved. This generalized Boussinesq system enjoys almost all the known properties of the 3D Navier-Stokes equations, including the incompressibility condition $(r^{m-2}u^r)_r + (r^{m-2}u^z)_z = 0$, the conservation of "total circulation" (density) Γ . Moreover, when $n = 3$ and $\nu_1 = \nu_2$, we can recover the 3D Navier-Stokes equations.

In our study, we use a small viscosity coefficient ($\nu_1 = 0.0006$) for Γ to generate a sharp shock like traveling wave for Γ that propagates toward the origin. This sharp shock front produces a Delta function like source term $(\Gamma^2/r^4)_z$ for the ω_1 equation. To stabilize the shearing instability induced by the sharp front of Γ , we apply a relatively large viscosity coefficient $\nu_2 = 10\nu_1$ in the ω_1 equation. This choice of viscosity coefficients generates a stable nearly self-similar traveling wave that produces a tornado like singularity at the origin with maximum vorticity increased by $1.4 \cdot 10^{30}$ by $\tau = 155$.

More specifically, we obtain the following scaling properties for the potential blowup solution:

$$\begin{aligned}\psi_1(t, r, z) &= \frac{\lambda(t)}{(T-t)^{1/2}} \Psi_1 \left(t, \frac{r}{\lambda(t)\sqrt{(T-t)}}, \frac{z}{\lambda(t)\sqrt{(T-t)}} \right), \\ u_1(t, r, z) &= \frac{1}{(T-t)} V_1 \left(t, \frac{r}{\lambda(t)\sqrt{(T-t)}}, \frac{z}{\lambda(t)\sqrt{(T-t)}} \right), \\ \omega_1(t, r, z) &= \frac{1}{\lambda(t)(T-t)^{3/2}} \Omega_1 \left(t, \frac{r}{\lambda(t)\sqrt{(T-t)}}, \frac{z}{\lambda(t)\sqrt{(T-t)}} \right),\end{aligned}$$

where $\lambda(t) = (1 + \epsilon|\log(T-t)|)^{-1/2}$ for some small constant ϵ . We normalize V_1 to satisfy $V_1(R(t), Z(t)) = 1$ and choose $n(t) = 4R(t)/Z(t) - 1$, which corresponds to $m = 1 + 2R(t)/Z(t)$. We observe that the dimension seems to settle to $n \approx 4.73$ by $\tau = 155$. This result is consistent with the finite time blowup of a diadic model for the Navier-Stokes for dimension $n > 4$ by Cheskidov in [17]. Since the maximum vorticity $\|\omega(t)\|_\infty$ has the same scaling as $\|u_1\|_\infty$, we conclude that $\|\omega(t)\|_\infty$ scales like $O((T-t)^{-1})$, which violates the Beale-Kato-Majda non-blowup criterion [1].

Denote $\xi = \frac{r}{\lambda(t)\sqrt{(T-t)}}$, $\eta = \frac{z}{\lambda(t)\sqrt{(T-t)}}$. We observe that as $t \rightarrow T$, the rescaled profile Ω_1 becomes increasingly flattened in an inner region centered at $(\xi, \eta) = (R_\omega, Z_\omega)$ where Ω_1 achieves its maximum. Moreover, we observe that $-\Delta_{(\xi, \eta)}\Omega_1$ roughly scales like $\lambda^2(t)\Omega_1$, which implies that the nearly self-similar profile enjoys a parabolic scaling within this inner region with domain size shrinking to zero in a logarithmic rate $\lambda(t)$ as $t \rightarrow T$. This scaling property plays an essential role in maintaining the balance between the source term $(\Gamma^2/r^4)_z$ and the diffusion term for ω_1 . Note that $(\Gamma^2/r^4)_z$ is the only nonlinear source term in the ω_1 equation. This makes it possible for the diffusion term of ω_1 to balance this Delta function like source term $(\Gamma^2/r^4)_z$.

1.3. The two-scale dynamic rescaling formulation. In order to capture the nearly self-similar blowup of the generalized Navier-Stokes equations and the generalized Boussinesq system, we need to control some unstable modes associated with the nearly self-similar blowup solution. These unstable modes are induced by the scaling instability due to the change of the scaling in the r and z directions, and the change of amplitude in the rescaled profile V_1 . In order to control the scaling instability due to the change of the scaling in the r and z directions, we need to fix the location $(R(\tau), Z(\tau))$ in which the solution V_1 achieves its maximum. We can achieve this by introducing a two-scale dynamic rescaling formulation, in which we rescale the r and z directions independently. This gives us an extra free scaling parameter to fix the location of the maximum of V_1 to be at $(\xi, \eta) = (R_0, 1)$.

1.4. The importance of resolving the far field solution. We remark that capturing the correct far field decay rate is essential to capture the correct scaling properties of the solution. Resolving the far field solution also plays an important role in capturing the slow growth rate of the L^n norm of

the velocity and the dynamic growth of $\|ru^r\|_\infty$. On the other hand, resolving the near field is also important since we need to compute accurately the location of the maximum of V_1 and its amplitude in order to enforce our normalization conditions. This poses a big challenge to our computational effort.

It is worth emphasizing the importance of using the conservative $(\Gamma, \omega_1, \psi_1)$ formulation in our two-scale dynamic rescaling formulation. This enables us to capture the nearly self-similar blowup. In our previous study, we had used an equivalent (u_1, ω_1, ψ_1) formulation, see (2.1a)-(2.1c). Although the (u_1, ω_1, ψ_1) formulation is equivalent to $(\Gamma, \omega_1, \psi_1)$ formulation at the continuous level, they are not equivalent at the discrete level. As a result, we lose the important total circulation conservation property at the discrete level if we use the (u_1, ω_1, ψ_1) formulation.

1.5. Confirming the blowup solution using various blowup criteria. We observe that the maximum vorticity for both the generalized Navier–Stokes with solution dependent viscosity and the generalized Boussinesq system with two constant viscosity coefficients scales like $O(1/(T-t))$. According to the Beale-Kato-Majda blow-up criterion [1], this would imply that both these equations with our initial data would develop a finite time singularity.

For the 3D Navier–Stokes equations, another quantity of interest is the growth rate of enstrophy $\|\omega(t)\|_{L^2}^2$. For the generalized Boussinesq system in n -dimension, we consider a generalized enstrophy $\|\omega(t)\|_{L^{n-1}}^{n-1}$. We observe a very rapid dynamic growth of the generalized enstrophy. A scaling analysis implies that $\int_0^t \|\omega(s)\|_{L^{n-1}}^q ds$ with $q = \frac{2(n-1)}{(n-2)}$ must blow up if the solution of the Navier–Stokes equations develops a self-similar blowup. We observe that $\int_0^t \|\omega(s)\|_{L^{n-1}}^q ds$ grows roughly like $\log(1/(T-t))$ for the generalized Boussinesq system with constant viscosity. This provides additional support that the generalized Boussinesq system with constant viscosity develops a finite time singularity.

We have also examined a generalized Ladyzhenskaya-Prodi-Serrin regularity criteria [50, 69, 72] that are based on the estimate of the $L_t^q L_x^p$ norm of the velocity with $n/p + 2/q \leq 1$. We study the cases of $(p, q) = (4n/3, 8)$, $(2n, 4)$, $(3n, 3)$, and $(\infty, 2)$ respectively. Denote by $\|\mathbf{u}(t)\|_{L^{p,q}} = \left(\int_0^t \|\mathbf{u}(s)\|_{L^p(\Omega)}^q ds\right)^{1/q}$. Our numerical results show that $\|\mathbf{u}(t)\|_{L^{p,q}}^q$ blows up roughly with a logarithmic rate, $O(|\log(T-t)|)$ for p large, e.g. $p = 2n, 3n, \infty$. This provides strong evidence for the development of a potential finite time singularity of the generalized Boussinesq system.

We have further investigated the nonblowup criteria based on the L^3 norm of the 3D velocity due to Escauriaza-Seregin-Sverak [30]. In the n -dimensional setting, we should consider the L^n norm of the velocity [67], which is scaling invariant. We observe a mild logarithmic growth of $\|\mathbf{u}(t)\|_{L^n}$ for the generalized Boussinesq system. Moreover, we examine the growth of the negative pressure and observe that $\| -p \|_\infty$ and $\|0.5|\nabla \mathbf{u}| + p\|_\infty$ blow up like $O(1/(T-t))$. This provides further evidence for the potential finite time singularity of the generalized Boussinesq system.

For the axisymmetric 3D Navier–Stokes equations, there are two more non-blowup criteria. In the work by Yau et al [10, 9] and Sverak et al [53], they exclude finite time blowup if the velocity field satisfies $\|\mathbf{u}\|_\infty \leq \frac{C}{\sqrt{T-t}}$ provided that $\|ru^r\|_\infty$ and $\|ru^z\|_\infty$ remain bounded for $r \geq r_0 > 0$. Our numerical study shows that $\|ru^r\|_\infty$ has a mild logarithmic growth in time. In the work by Wei [78] (see also [55]), finite time blowup of the 3D axisymmetric Navier–Stokes is excluded if the condition $|\log(r)|^{3/2}|\Gamma(t, r, z)| \leq 1$ for $r \leq \delta_0 < 1/2$. If we assume that their key estimate based on the Hardy inequality still holds, their result should also apply to the generalized Boussinesq system. Our numerical result shows that $\max_{r \leq \delta_0} |\log(r)|^{3/2}|\Gamma(t, r, z)|$ can grow roughly like $O(|\log(T-t)|)$ as $t \rightarrow T$. This provides further evidence for the finite time blowup of the generalized Boussinesq system.

1.6. Review of previous works. For the 3D Navier–Stokes equations, the partial regularity result due to Caffarelli–Kohn–Nirenberg [6] is one of the best known results (see a simplified proof by Lin [57]). This result implies that any potential singularity of the axisymmetric Navier–Stokes equations must occur on the symmetry axis. There have been some very interesting theoretical developments regarding

the lower bound on the blow-up rate for axisymmetric Navier–Stokes equations [10, 9, 53]. Another interesting development is a result due to Tao [75] who proposed an averaged three-dimensional Navier–Stokes equation that preserves the energy identity, but blows up in finite time.

There have been a number of theoretical developments for the 3D incompressible Euler equations, including the Beale–Kato–Majda blow-up criterion [61], the geometric non-blow-up criterion due to Constantin–Fefferman–Majda [20] and its Lagrangian analog due to Deng–Hou–Yu [23]. Inspired by their work on the vortex sheet singularity [8], Caffisch and Siegel have studied complex singularity for 3D Euler equation, see [7, 73], and also [68] for the complex singularities for 2D Euler equation.

In 2021, Elgindi [26] (see also [27]) proved an exciting result: the 3D axisymmetric Euler equations develop a finite time singularity for a class of $C^{1,\alpha}$ initial velocity with no swirl and a very small α . There have been a number of interesting theoretical results inspired by the Hou–Lou blowup scenario [59, 60], see e.g. [52, 18, 19, 51, 13, 16, 15] and the excellent survey article [49]. We remark that Huang–Qin–Wang–Wei recently proved the existence of exact self-similar blowup profiles for the gCML model and the Hou–Luo model by using a purely analytic fixed point method in [46, 45].

There has been substantial progress on singularity formation of 3D Euler equations in recent years. In [14, 12], Chen and Hou have established a computer-assisted proof of finite time blowup for the 2D Boussinesq and the 3D axisymmetric Euler equations with boundary and smooth initial data by proving the nonlinear stability of the blowup profile in the dynamic rescaling equations. In [28, 29], Elgindi–Pasqualotto established blowup of 2D Boussinesq and 3D Euler equations (with large swirl) with $C^{1,\alpha}$ velocity and without boundary. In [22], Cordoba–Martinez–Zoroa–Zheng developed a new method different from the above self-similar approach to establish blowup of axisymmetric Euler equations with no swirl and with $\mathbf{u}(t) \in C^\infty(R^3 \setminus O) \cap C^{1,\alpha} \cap L^2$. In [11], Chen proved that such a blowup result can also be established by the self-similar approach. By adding an external force f uniformly bounded in $C^{1,1/2^-}$ up to the blowup time, the authors of [21] established blowup of 3D Euler with smooth velocity.

There have been relatively few papers on the numerical study regarding the potential blow-up of the 3D Navier–Stokes equations. We refer to a recent survey paper [70] by Protas on systematic search for potential singularities of the Navier–Stokes equations by solving PDE optimization problems. It concludes that "No evidence for singularity formation was found in extreme Navier–Stokes flows constructed in this manner in three dimensions." There were a number of attempts to look for potential Euler singularities numerically, see [33, 25, 2, 48, 40, 41, 59, 60, 3, 37, 38, 77]. We refer to a review article [32] for more discussions on potential Euler singularities.

The rest of the paper is organized as follows. In Section 2, we derive the generalized Navier–Stokes equation and perform the energy estimates for the generalized Navier–Stokes equations and the generalized Boussinesq system. In Section 3, we introduce our two-scale dynamic rescaling formulation. In Section 4, we investigate the self-similar blowup of the generalized Navier–Stokes equations with solution dependent viscosity. Section 5 is devoted to the nearly self-similar blowup of the generalized Boussinesq system with constant viscosity. Some concluding remarks are made in Section 6.

2. DERIVATION OF THE GENERALIZED NAVIER–STOKES EQUATIONS AND ENERGY ESTIMATES

We first review the 3D axisymmetric Navier–Stokes equations. Let u^θ , ω^θ , and ψ^θ be the angular velocity, angular vorticity and angular stream function, respectively. We consider the following reformulated axisymmetric Navier–Stokes equations derived by Hou–Li in [39]:

$$u_{1,t} + u^r u_{1,r} + u^z u_{1,z} = 2u_1 \psi_{1,z} + \nu_1 \left(u_{1,rr} + \frac{3}{r} u_{1,r} + u_{1,zz} \right), \quad (2.1a)$$

$$\omega_{1,t} + u^r \omega_{1,r} + u^z \omega_{1,z} = (u_1^2)_z + \nu_2 \left(\omega_{1,rr} + \frac{3}{r} \omega_{1,r} + \omega_{1,zz} \right), \quad (2.1b)$$

$$-\left(\partial_r^2 + \frac{3}{r}\partial_r + \partial_z^2\right)\psi_1 = \omega_1, \quad (2.1c)$$

where $u^r = -r\psi_{1,z}$, $u^z = 2\psi_1 + r\psi_{1,r}$, $u_1 = u^\theta/r$, $\omega_1 = \omega^\theta/r$, $\psi_1 = \psi^\theta/r$.

2.1. A brief review of the adaptive mesh computation. In [35, 36], the author studied the potential singular behavior of the axisymmetric Euler and Navier–Stokes equations using the following initial condition:

$$u_1(0, r, z) = \frac{12000(1 - r^2)^{18} \sin(2\pi z)}{1 + 12.5(\sin(\pi z))^2}, \quad \omega_1(0, r, z) = 0, \quad r \leq 1. \quad (2.2)$$

The flow is completely driven by large swirl initially. The other two velocity components are set to zero initially. Note that u_1 is an odd and periodic function of z with period 1. The oddness of u_1 induces the oddness of ω_1 dynamically through the vortex stretching term in the ω_1 -equation. It is worth emphasizing that the specific power 18 is important, which determines the ratio of the scales along the r and z directions and enforces a rapid decay near the boundary $r = 1$. The specific form of the denominator is also important. It breaks the even symmetry of $\sin(2\pi z)$ with respect to $z = 1/4$ along the z direction with a bias toward $z = 0$. This initial condition generates a solution that has comparable scales along the r and z directions, leading to an one-scale traveling solution moving toward the origin.

We will impose a periodic boundary condition in z with period 1 and no-slip no-flow boundary condition at $r = 1$. Since $u^\theta, \omega^\theta, \psi^\theta$ is an odd function of r [58], u_1, ω_1, ψ_1 is an even function of r . Thus, we impose the following pole conditions: $u_{1,r}(t, 0, z) = \omega_{1,r}(t, 0, z) = \psi_{1,r}(t, 0, z) = 0$. To numerically compute the potential singularity formation of the equations (2.1) with initial condition (2.2), we adopt the numerical methods developed in [37, 38]. In particular, we design an adaptive mesh by constructing two adaptive mesh maps for r and z explicitly. The computation is performed in the transformed domain using a uniform mesh. When we map back to the physical domain, we obtain a highly adaptive mesh. We refer to Appendix A in [38] for more detailed discussions.

We will study the nearly self-similar blowup of the generalized axisymmetric Navier–Stokes equations using a novel two-scale dynamic rescaling formulation. We will use the late stage solution obtained by the adaptive mesh computation in [36] at the time T_1 by which the maximum vorticity has increased by a factor of 10^6 . We will rescale the solution at T_1 using the parabolic scaling invariant property and apply a soft cut-off to the far field to obtain an initial condition for the dynamic rescaling formulation.

2.2. Derivation of the generalized Navier–Stokes equations. We first derive the generalized Navier–Stokes equations. In [43, 44], we performed numerical study of the finite time self-similar blowup of the axisymmetric Euler equations with no swirl in 3 and higher space dimensions for C^α initial vorticity for a wide range of α . We first define the n -dimensional cylindrical unit vectors

$$\begin{aligned} e_r &= (\cos \theta_1, \sin \theta_1 \cos \theta_2, \dots, \sin \theta_1, \dots \cos \theta_{n-2}, \sin \theta_1 \dots \sin \theta_{n-2}, 0), \\ e_{\theta_1} &= (-\sin \theta_1, \cos \theta_1 \cos \theta_2, \dots, \cos \theta_1, \dots \cos \theta_{n-2}, \cos \theta_1 \dots \sin \theta_{n-2}, 0), \\ e_{\theta_{n-2}} &= (0, 0, \dots, -\sin \theta_{n-2}, \cos \theta_{n-2}, 0), \\ e_z &= (0, 0, \dots, 1). \end{aligned}$$

Let us assume that the only nontrivial swirl velocity is in θ_1 variable, denoted as u^{θ_1} and $u^{\theta_j} \equiv 0$ for $j = 2, 3, \dots, n-2$. We call the velocity field \mathbf{u} axisymmetric if it admits the following expression:

$$\mathbf{u} = u^r(t, r, z)e_r + u^{\theta_1}(t, r, z)e_{\theta_1} + u^z(t, r, z)e_z.$$

Using the calculus on curvilinear coordinate, we obtain

$$\nabla \cdot \mathbf{u} = \frac{(r^{n-2}u^r)_r}{r^{n-2}} + \frac{(n-3)\cot(\theta_1)}{r}u^{\theta_1} + \frac{(r^{n-2}u^z)_z}{r^{n-2}}.$$

We will denote θ_1 as θ from now on. Similar to the 3D axisymmetric Euler or Navier–Stokes equations, we introduce the angular vorticity ω^θ and angular stream function ψ^θ by defining $\omega^\theta = u_r^z - u_z^r$ and $-\Delta\psi^\theta = \omega^\theta$. Using ψ^θ , we can define u^r and u^z in terms of ψ^θ as follows:

$$u^r = -\frac{(r^{n-2}\psi^\theta)_z}{r^{n-2}}, \quad u^z = \frac{(r^{n-2}\psi^\theta)_r}{r^{n-2}}. \quad (2.3)$$

In order to satisfy the divergence free condition, we modify the velocity field as follows:

$$\mathbf{u} = u^r(t, r, z)e_r + u^z(t, r, z)e_z.$$

Moreover, we treat the total circulation $\Gamma = ru^\theta$ as "density" and still define $u_1 = u^\theta/r$, $\omega_1 = \omega^\theta/r$ and $\psi_1 = \psi^\theta/r$. Our generalized n -dimensional axisymmetric Navier–Stokes equations are given as follows:

$$\Gamma_t + u^r\Gamma_r + u^z\Gamma_z = \nu \left(\Gamma_{rr} + \frac{(n-4)}{r}\Gamma_r + \frac{(6-2n)}{r^2}\Gamma + \Gamma_{zz} \right), \quad (2.4a)$$

$$\omega_{1,t} + u^r\omega_{1,r} + u^z\omega_{1,z} = (u_1^2)_z - (n-3)\psi_{1,z}\omega_1 + \nu \left(\omega_{1,rr} + \frac{n}{r}\omega_{1,r} + \omega_{1,zz} \right), \quad (2.4b)$$

$$-\left(\partial_r^2 + \frac{n}{r}\partial_r + \partial_z^2 \right) \psi_1 = \omega_1, \quad (2.4c)$$

where $u^r = -r\psi_{1,z}$, $u^z = (n-1)\psi_1 + r\psi_{1,r}$. The divergence free condition $\nabla \cdot \mathbf{u} = \frac{(r^{n-2}u^r)_r}{r^{n-2}} + \frac{(r^{n-2}u^z)_z}{r^{n-2}} = 0$ is satisfied exactly. The generalized Navier–Stokes equations still conserve the energy, see the derivation in the next subsection. When $n = 3$, we recover the 3D axisymmetric Navier–Stokes equations.

To derive the generalized Boussinesq system (1.2), we again treat Γ as density and remove $(n-3)\psi_{1,z}\omega_1$ from the generalized Navier–Stokes equations. We define the velocity as $u^r = -r\psi_{1,z}$, $u^z = (m-1)\psi_1 + r\psi_{1,r}$ with $m = (n+3)/2$ and $n = 4R(t)/Z(t) - 1$. We will show that this generalized Boussinesq system satisfies energy conservation in the next subsection. The blowup is driven by the density variation of Γ , which develops a traveling wave with a sharp front approaching to the origin.

2.3. Energy estimates for the generalized Navier–Stokes equations. In this subsection, we will derive the energy estimates for both the generalized Navier–Stokes equations and the generalized Boussinesq system for a fixed dimension n . We first rewrite the Γ -equation in terms of u_1 as follows:

$$u_{1,t} + u^r u_{1,r} + u^z u_{1,z} = 2u_1 \psi_{1,z} + \nu_1 \left(u_{1,rr} + \frac{n}{r} u_{1,r} + u_{1,zz} \right). \quad (2.5)$$

To perform energy estimates for the generalize Navier–Stokes equations (2.4), we multiply the u_1 -equation (2.5) by $u_1 r^n dr dz$ and integrate over the whole domain. Similarly, we multiply equation (2.4b) for ω_1 and equation (2.4c) for ψ_1 by $\psi_1 r^n dr dz$, and integrate over the whole domain. Using the divergence form of the diffusion operator,

$$u_{1,rr} + \frac{n}{r} u_{1,r} + u_{1,zz} = \left(\frac{(r^n u_{1,r})_r}{r^n} + u_{1,zz} \right),$$

we perform integration by parts to obtain

$$\begin{aligned} \int u_1 (u_{1,rr} + \frac{n}{r} u_{1,r} + u_{1,zz}) r^n dr dz &= - \int |\nabla u_1|^2 r^n dr dz, \\ - \int \psi_1 (\psi_{1,rr} + \frac{n}{r} \psi_{1,r} + \psi_{1,zz}) r^n dr dz &= \int |\nabla \psi_1|^2 r^n dr dz, \\ \int \psi_1 (\omega_{1,rr} + \frac{n}{r} \omega_{1,r} + \omega_{1,zz}) r^n dr dz &= - \int |\Delta \psi_1|^2 r^n dr dz, \end{aligned}$$

where we have used $-\Delta\psi_1 = \omega_1$. There are no contributions from the boundary when we perform integration by parts since ψ_1 , u_1 and ω_1 are odd function of z and even function of r . Using $u^r = -(r^{n-1}\psi_1)_z/r^{n-2}$, $u^z = (r^{n-1}\psi_1)_r/r^{n-2}$ and the incompressibility condition, we get

$$\begin{aligned} & \int u_1(-u^r u_{1,r} - u^z u_{1,z} + 2\psi_{1,z} u_1) r^n dr dz \\ &= \int \left(\frac{1}{2} (r^{n-1}\psi_1)_z (u_1^2)_r - \frac{1}{2} (r^{n-1}\psi_1)_r (u_1^2)_z \right) r^2 dr dz + \int 2\psi_{1,z} u_1^2 r^n dr dz \\ &= \int \psi_{1,z} u_1^2 r^n dr dz. \end{aligned}$$

Similarly, we obtain by integration by parts that

$$\begin{aligned} & \int \psi_1(-u^r \omega_{1,r} - u^z \omega_{1,z} + (u_1^2)_z - (n-3)\psi_{1,z} \omega_1) r^n dr dz \\ &= \int (\psi_1 (r^{n-1}\psi_1)_z \omega_{1,r} - \psi_1 (r^{n-1}\psi_1)_r \omega_{1,z}) r^2 dr dz + \int (-\psi_{1,z} u_1^2 - (n-3)\psi_1 \psi_{1,z} \omega_1) r^n dr dz \\ &= (n-3) \int \psi_1 \psi_{1,z} \omega_1 r^n dr dz - \int (\psi_{1,z} u_1^2 + (n-3)\psi_1 \psi_{1,z} \omega_1) r^n dr dz \\ &= - \int \psi_{1,z} u_1^2 r^n dr dz. \end{aligned}$$

By adding the above two estimates, we observe that the right hand side terms cancel each other. Thus, we have

$$\frac{1}{2} \frac{d}{dt} \int (u_1^2 + |\nabla\psi_1|^2) r^n dr dz = -\nu \int (|\nabla u_1|^2 + |\Delta\psi_1|^2) r^n dr dz.$$

In terms of the original physical variables, we get by a direct computation that

$$\int (u_1^2 + |\nabla\psi_1|^2) r^n dr dz = \int (|u^\theta|^2 + |u^r|^2 + |u^z|^2) r^{n-2} dr dz,$$

which is the familiar kinetic energy $\int |\mathbf{u}|^2 r^{n-2} dr dz$ in n dimensions. The damping term from the viscous term can be shown to be equivalent to $-\nu \int (|\nabla\mathbf{u}|^2) r^{n-2} dr dz$.

We can perform a similar energy estimate for the generalized Boussinesq system. As we can see from our above energy estimate, the term $-(n-3)\psi_{1,z}\omega_1$ from the ω_1 equation plays an important role in canceling the contribution from the advection terms. Since we drop the term $-(n-3)\psi_{1,z}\omega_1$ in the ω_1 equation in the generalized Boussinesq system, we need to change the weight in our energy estimate to cancel the contribution from the advection terms. We proceed as follows:

$$\begin{aligned} & \int u_1(-u^r u_{1,r} - u^z u_{1,z} + 2\psi_{1,z} u_1) r^n dr dz \\ &= \int \left(\frac{1}{2} (r^{m-1}\psi_1)_z (u_1^2)_r - \frac{1}{2} (r^{m-1}\psi_1)_r (u_1^2)_z \right) r^{n-m+2} dr dz + \int 2\psi_{1,z} u_1^2 r^n dr dz \\ &= \frac{(5-m)}{2} \int \psi_{1,z} u_1^2 r^n dr dz = \frac{(7-n)}{4} \int \psi_{1,z} u_1^2 r^n dr dz. \end{aligned}$$

Similarly, we obtain by integration by parts that

$$\int \psi_1(-u^r \omega_{1,r} - u^z \omega_{1,z} + (u_1^2)_z) r^n dr dz$$

$$\begin{aligned}
&= \int (\psi_1(r^{m-1}\psi_1)_z\omega_{1,r} - \psi_1(r^{m-1}\psi_1)_r\omega_{1,z}) r^{n-m+2} dr dz - \int \psi_{1,z}u_1^2 r^n dr dz \\
&= (2m - 3 - n) \int \psi_1\psi_{1,z}\omega_1 r^n dr dz - \int \psi_{1,z}u_1^2 r^n dr = - \int \psi_{1,z}u_1^2 r^n dr dz,
\end{aligned}$$

where we have used $m = (n + 3)/2$ to cancel the first term on the right hand side in the second to the last step. Since we assume $n < 7$, we obtain the following generalized energy estimate by forming a linear combination of the two energy terms to cancel the right hand sides

$$\frac{1}{2} \frac{d}{dt} \int (u_1^2 + \frac{(7-n)}{4} |\nabla\psi_1|^2) r^n dr dz = -\nu_1 \int |\nabla u_1|^2 r^n dr dz - \nu_2 \frac{(7-n)}{4} \int |\Delta\psi_1|^2 r^n dr dz.$$

We can further express $\int (u_1^2 + \frac{(7-n)}{4} |\nabla\psi_1|^2) r^n dr dz$ as $\int ((u^\theta)^2 + \frac{(7-n)}{4} (|u^r|^2 + |u^z|^2)) r^{n-2} dr dz$.

3. A NOVEL TWO-SCALE DYNAMIC RESCALING FORMULATION

In this subsection, we introduce a novel two-scale dynamic rescaling formulation to study potential nearly self-similar blowup solution of the generalized Navier–Stokes equations. The dynamic rescaling formulation was introduced in [63, 54] to study the self-similar blowup of the nonlinear Schrödinger equations. This formulation is also called the modulation technique in the literature and has been developed by Merle, Raphael, Martel, Zaag, Soffer, Weinstein, and others. It has been a very effective tool to analyze the formation of singularities for many problems like the nonlinear Schrödinger equation [74, 47, 64], compressible Euler equations [4, 5], the nonlinear wave equation [66], the nonlinear heat equation [65], the generalized KdV equation [62], and other dispersive problems. Recently, this method has been applied to study singularity formation in incompressible fluids [13, 26].

We first define the following dynamically rescaled profiles and the rescaled time variable τ .

$$\begin{aligned}
\tilde{u}_1(\tau, \xi, \eta) &= C_u(\tau)u_1(t(\tau), C_{lr}(\tau)\xi, C_{lz}(\tau)\eta), \\
\tilde{\omega}_1(\tau, \xi, \eta) &= C_\omega(\tau)\omega_1(t(\tau), C_{lr}(\tau)\xi, C_{lz}(\tau)\eta), \\
\tilde{\psi}_1(\tau, \xi, \eta) &= C_\psi(\tau)\psi_1(t(\tau), C_{lr}(\tau)\xi, C_{lz}(\tau)\eta),
\end{aligned}$$

where $\xi = r/C_{lr}$, $\eta = z/C_{lz}$,

$$C_u(\tau) = e^{\int_0^\tau c_u(s)ds}, \quad C_\omega(\tau) = e^{\int_0^\tau c_\omega(s)ds}, \quad C_\psi(\tau) = e^{\int_0^\tau c_\psi(s)ds},$$

and

$$C_{lr}(\tau) = e^{-\int_0^\tau c_{lr}(s)ds}, \quad C_{lz}(\tau) = e^{-\int_0^\tau c_{lz}(s)ds}, \quad t(\tau) = \int_0^\tau C_\psi(s)C_{lz}(s)ds.$$

Here τ is the rescaled time variable satisfying $d\tau/dt = (C_\psi C_{lz})^{-1}$. Then, the generalized n -dimensional axisymmetric Navier–Stokes equations in the $\tilde{\psi}_1$, \tilde{u}_1 , $\tilde{\omega}_1$ variables can be described by the following two-scale dynamic rescaling equations

$$\begin{aligned}
\tilde{u}_{1,\tau} + c_{lr}\xi\tilde{u}_{1,\xi} + c_{lz}\eta\tilde{u}_{1,\eta} + \tilde{\mathbf{u}} \cdot \nabla_{(\xi,\eta)}\tilde{u}_1 &= c_u\tilde{u}_1 + 2\tilde{u}_1\tilde{\psi}_{1,\eta} + \frac{\nu_1 C_\psi}{C_{lz}} \Delta\tilde{u}, \\
\tilde{\omega}_{1,\tau} + c_{lr}\xi\tilde{\omega}_{1,\xi} + c_{lz}\eta\tilde{\omega}_{1,\eta} + \tilde{\mathbf{u}} \cdot \nabla_{(\xi,\eta)}\tilde{\omega}_1 &= c_\omega\tilde{\omega}_1 + (\tilde{u}_1^2)_\eta - (n-3)\tilde{\psi}_{1,\eta}\tilde{\omega}_1 + \frac{\nu_2 C_\psi}{C_{lz}} \Delta\tilde{\omega}, \\
-\Delta\tilde{\psi}_1 &= \tilde{\omega}_1, \quad \Delta = \left(\delta^2 \partial_\xi^2 + \delta^2 \frac{n}{\xi} \partial_\xi + \partial_\eta^2 \right),
\end{aligned}$$

where $\delta = C_{lz}(\tau)/C_{lr}(\tau)$ and the rescaled velocity field is given by $\tilde{\mathbf{u}} = (\tilde{u}^\xi, \tilde{u}^\eta)$, $\tilde{u}^\xi = -\xi\tilde{\psi}_{1,\eta}$, $\tilde{u}^\eta = (n-1)\tilde{\psi}_1 + \xi\tilde{\psi}_{1,\xi}$, and the scaling parameters $(c_{lz}, c_{lr}, c_\psi, c_u, c_\omega)$ satisfy the rescaling relationship

$$c_\psi = c_u + c_{lz}, \quad c_\omega = c_u - c_{lz}. \quad (3.1)$$

We refer to the excellent survey paper [24] for more discussion of high dimensional Euler equations (see also [44]). In the case of the generalized Boussinesq system, we drop $(n-3)\tilde{\psi}_{1,\eta}\tilde{\omega}_1$ from the $\tilde{\omega}_1$ equation, and change the velocity field to $u^r = -(r^{m-2}\psi^\theta)_z/r^{m-2}$, $u^z = (r^{m-2}\psi^\theta)_r/r^{m-2}$ with $m = (n+3)/2$. We have three free parameters c_{lr} , c_{lz} and c_u to choose to enforce the normalization conditions that \tilde{u}_1 achieves its maximum at $(\xi, \eta) = (R_0, 1)$ with $R_0 = 3.6927$ and $\|\tilde{u}_1\|_\infty$ being fixed to be 1. We remark that (R_ω, Z_ω) converges to a fixed position (R_ω, Z_ω) as τ increases.

If the scaling parameters converge to a constant value as $\tau \rightarrow \infty$,

$$(c_{lz}(\tau), c_{lr}(\tau), c_\psi(\tau), c_u(\tau), c_\omega(\tau)) \rightarrow (c_{lz}, c_{lr}, c_\psi, c_u, c_\omega),$$

we can obtain the actual blowup rate in the physical time variable by inverting the mapping from τ back to t . To simplify the derivation, we assume that $(c_{lz}(\tau), c_{lr}(\tau), c_\psi(\tau), c_u(\tau), c_\omega(\tau))$ are time independent. Then we obtain the following asymptotic scaling results:

$$C_\psi(\tau) = e^{c_\psi\tau}, \quad C_{lz}(\tau) = e^{-c_{lz}\tau},$$

which implies that

$$t(\tau) = \int_0^\tau C_\psi(s)C_{lz}(s)ds = \frac{1}{c_\psi - c_{lz}}(e^{(c_\psi - c_{lz})\tau} - 1).$$

By inverting this relationship, we obtain

$$\tau = \frac{1}{c_{lz} - c_\psi} \log\left(\frac{1}{T-t}\right),$$

where $T = \frac{1}{c_{lz} - c_\psi}$. By substituting $\tau = \frac{|\log(T-t)|}{c_{lz} - c_\psi}$ back to C_u , C_ω , C_{lz} etc and using $c_\psi = c_u + c_{lz}$ and $c_\omega = c_u - c_{lz}$, we obtain the following scaling formula:

$$C_{lz}(\tau) = (T-t)^{\widehat{c}_{lz}}, \quad C_{lr}(\tau) = (T-t)^{\widehat{c}_{lr}},$$

where $\widehat{c}_{lz} = c_{lz}/(c_{lz} - c_\psi)$ and $\widehat{c}_{lr} = c_{lr}/(c_{lz} - c_\psi)$. The blowup rates are given by

$$\frac{1}{C_u(\tau)} = \frac{1}{(T-t)}, \quad \frac{1}{C_\omega(\tau)} = \frac{1}{(T-t)^{1+\widehat{c}_{lz}}}, \quad \frac{1}{C_\psi(\tau)} = \frac{1}{(T-t)^{1-\widehat{c}_{lz}}},$$

where $\widehat{c}_\omega = c_\omega/(c_{lz} - c_\psi) = -1 - \widehat{c}_{lz}$ and $\widehat{c}_\psi = c_\psi/(c_{lz} - c_\psi) = -1 + \widehat{c}_{lz}$. In our computation, we monitor closely these normalized scaling exponents \widehat{c}_ω , \widehat{c}_ψ , \widehat{c}_{lz} and \widehat{c}_{lr} to study their scaling properties.

As we mentioned before, we will use the conservative $(\Gamma, \omega_1, \psi_1)$ formulation in our computation. Using the relationship $\Gamma = r^2 u_1$, we can obtain an equivalent dynamic rescaling formulation for $(\Gamma, \omega_1, \psi_1)$ as follows:

$$\begin{aligned} \widetilde{\Gamma}_\tau + c_{lr}\xi\widetilde{\Gamma}_\xi + c_{lz}\eta\widetilde{\Gamma}_\eta + \widetilde{\mathbf{u}} \cdot \nabla_{(\xi,\eta)}\widetilde{\Gamma} &= c_\Gamma\widetilde{\Gamma} + \frac{\nu_1 C_\psi}{C_{lz}}\widetilde{\Delta}\widetilde{\Gamma}, \\ \widetilde{\omega}_{1,\tau} + c_{lr}\xi\widetilde{\omega}_{1,\xi} + c_{lz}\eta\widetilde{\omega}_{1,\eta} + \widetilde{\mathbf{u}} \cdot \nabla_{(\xi,\eta)}\widetilde{\omega}_1 &= c_\omega\widetilde{\omega}_1 + (\widetilde{u}_1^2)_\eta + (3-n)\widetilde{\psi}_{1,\eta}\widetilde{\omega}_1 + \frac{\nu_2 C_\psi}{C_{lz}}\Delta\widetilde{\omega}, \\ -\Delta\widetilde{\psi}_1 &= \widetilde{\omega}_1, \quad \Delta = \left(\delta^2\partial_\xi^2 + \delta^2\frac{n}{\xi}\partial_\xi + \partial_\eta^2\right), \end{aligned}$$

where $c_\Gamma = c_u + 2c_{lr} = 2(c_{lr} - c_{lz})$ and

$$\widetilde{\Delta}\widetilde{\Gamma} = \left(\delta^2\partial_\xi^2\widetilde{\Gamma} + \delta^2\frac{n-4}{\xi}\partial_\xi\widetilde{\Gamma} + \delta^2\frac{6-2n}{\xi^2}\widetilde{\Gamma} + \partial_\eta^2\widetilde{\Gamma}\right).$$

We still choose c_{lr} and c_{lz} to enforce that \tilde{u}_1 achieves its maximum at $(\xi, \eta) = (R_0, 1)$ and choose c_u to fix the maximum value of \tilde{u}_1 to be 1.

We also expand the domain size by $R(\tau)^{-1/5}$ and $Z(\tau)^{-1/5}$ in the r and z directions, respectively and apply the homogeneous Neumann boundary conditions for the stream function $\tilde{\psi}_1$, $\tilde{\Gamma}$ and $\tilde{\omega}_1$. In the case of the generalized axisymmetric Boussinesq system with two constant viscosity coefficients, we have $(R(\tau), Z(\tau)) = (3.3 \cdot 10^{-15}, 6.2 \cdot 10^{-16})$ by the end of our computation. The domain size has increased to $[0, 3 \cdot 10^7] \times [0, 1.65 \cdot 10^7]$ from the initial domain size of $O(10^4)$.

In the case of the generalized Navier–Stokes equations with solution dependent viscosity $\nu(\tau) = \nu_0 \|u_1\|_\infty Z(t)^2$, we note that $\|u_1\|_\infty Z(t)^2 = \|\tilde{u}_1\|_\infty = C_{lz}/C_\psi$. Thus, we have $\frac{\nu C_\psi}{C_{lz}} = \nu_0$. As a result, the dynamic rescaling formulation is the same as that for the generalized axisymmetric Navier–Stokes equations with a constant viscosity ν_0 . If $c_{lz} \rightarrow c_l$ and $c_{lr} \rightarrow c_l$, then we have $\delta(\tau) \rightarrow \lambda_0$. In our computation, we obtain $\lambda_0 \approx 0.914$. If the dynamic rescaled solution converges to a steady state, we can rescale the ξ variable to ξ/λ_0 to obtain an one-scale solution with $\delta = 1$ and $c_{lr} = c_{lz} \equiv c_l$. If the solution of the dynamic rescaling equations converges to a steady state, the steady state satisfies the following self-similar equations:

$$(c_l \xi, c_l \eta) \cdot \nabla_{(\xi, \eta)} \tilde{\Gamma} + \tilde{\mathbf{u}} \cdot \nabla_{(\xi, \eta)} \tilde{\Gamma} = \nu_0 \Delta \tilde{\Gamma}, \quad (3.2)$$

$$(c_l \xi, c_l \eta) \cdot \nabla_{(\xi, \eta)} \tilde{\omega}_{1, \eta} + \tilde{\mathbf{u}} \cdot \nabla_{(\xi, \eta)} \tilde{\omega}_1 = c_\omega \tilde{\omega}_1 + (\tilde{u}_1^2)_\eta - (n-3) \tilde{\psi}_{1, \eta} \tilde{\omega}_1 + \nu_0 \Delta \tilde{\omega}, \quad (3.3)$$

$$-\Delta \tilde{\psi}_1 = \tilde{\omega}_1, \quad \Delta = - \left(\partial_\xi^2 + \frac{n}{\xi} \partial_\xi + \partial_\eta^2 \right), \quad (3.4)$$

where we have used $c_r = 2(c_{lr} - c_{lz}) = 0$. In our study, we observe that c_l and n decrease as ν_0 decreases. It would be interesting to solve the self-similar equations directly with ν_0 as a continuation parameter. Due to the total circulation conservation of the generalized Euler equations, we expect to have $c_l \rightarrow 1/2$ and $n \rightarrow 3$ in the limit $\nu_0 \rightarrow 0$.

3.1. The operator splitting strategy. We will adopt an operator splitting strategy developed in [?] to enforce the normalization conditions. To enforce the normalization conditions accurately at every time step, we utilize the operator splitting method. We denote by $\mathbf{v} = (\tilde{\Gamma}, \tilde{\omega}_1)$. We will split the time evolution of \mathbf{v} into two parts:

$$\mathbf{v}_\tau = F(\mathbf{v}) + G(\mathbf{v}),$$

where $F(\mathbf{v})$ contains the original terms in the generalized Navier–Stokes equations and $G(\mathbf{v})$ contains the linear terms that control the rescaling, i.e. $G(\mathbf{v}) = -c_{lr} \xi \mathbf{v}_\xi - c_{lz} \eta \mathbf{v}_\eta + c_v \mathbf{v}$. We view $\tilde{\psi}_1$ as a function of $\tilde{\omega}_1$ through the Poisson equation. The operator splitting method allows us to solve the dynamic rescaling formulation by solving $\mathbf{v}_\tau = F(\mathbf{v})$ and $\mathbf{v}_\tau = G(\mathbf{v})$ alternatively. We can use the forward Euler method to solve $\mathbf{v}_\tau = F(\mathbf{v})$. In the second step, we can obtain a closed form solution to $\mathbf{v}_\tau = G(\mathbf{v})$ as follows:

$$\mathbf{v}(\tau, \xi, \eta) = C_v(\tau) \mathbf{v}(0, C_{lr} \xi, C_{lz} \eta),$$

where $C_v = \exp\left(\int_0^\tau c_v(s) ds\right)$, $C_{lr} = \exp\left(-\int_0^\tau c_{lr}(s) ds\right)$ and $C_{lz} = \exp\left(-\int_0^\tau c_{lz}(s) ds\right)$. In the first step, solving $\mathbf{v}_\tau = F(\mathbf{v})$ will violate the normalization conditions. But we will correct this error in the second step by solving $\mathbf{v}_\tau = G(\mathbf{v})$ with a smart choice of C_v , C_{lr} and C_{lz} . In other words, at every time step when we solve $\mathbf{v}_\tau = G(\mathbf{v})$, we can exactly enforce the normalization conditions of fixing the location of the maximum of \tilde{u}_1 to be at $(R_0, 1)$ by rescaling the ξ and η coordinates. We could also adopt Strang's splitting method to improve the splitting scheme to second order accuracy.

4. BLOWUP OF THE GENERALIZED NAVIER-STOKES EQUATIONS WITH SOLUTION DEPENDENT VISCOSITY

In this section, we will investigate the asymptotically self-similar blowup of the generalized Navier–Stokes equations with solution dependent viscosity. It turns out that the choice of the viscosity coefficient plays a crucial role in generating a stable and self-similar blowup of the generalized Navier–Stokes equations. In our study, we choose $\nu = \nu_0 \|u_1\|_\infty Z(t)^2$ with $\nu_0 = 0.006$. Here $(R(t), Z(t))$ is

the position where u_1 achieves its maximum. Note that $\|u_1\|_\infty Z(t)^2$ is scaling invariant. This choice of viscosity is to enforce the balance between the vortex stretching terms and the diffusion terms for both the u_1 and ω_1 equations. Another way to interpret this solution dependent viscosity is that it is chosen such that the cell Reynolds number is finite and independent of the small scales of the physical solution.

An important consequence of this choice of viscosity is that the self-similar profile of the blowup solution satisfies the generalized self-similar Navier–Stokes equations with *constant viscosity coefficient* ν_0 . This explains why we can maintain the balance between the vortex stretching term and the diffusion term in the self-similar space variables $\xi = r/C_{lr}$ and $\eta = z/C_{lz}$.

4.1. Rapid growth of maximum vorticity. In this subsection, we investigate how the profiles of the solution evolve in time. We will use the numerical results computed on the adaptive mesh using resolution $(n_1, n_2) = (1024, 1024)$. We have computed the numerical solution up to time $\tau = 185$ when the solution is still well resolved.

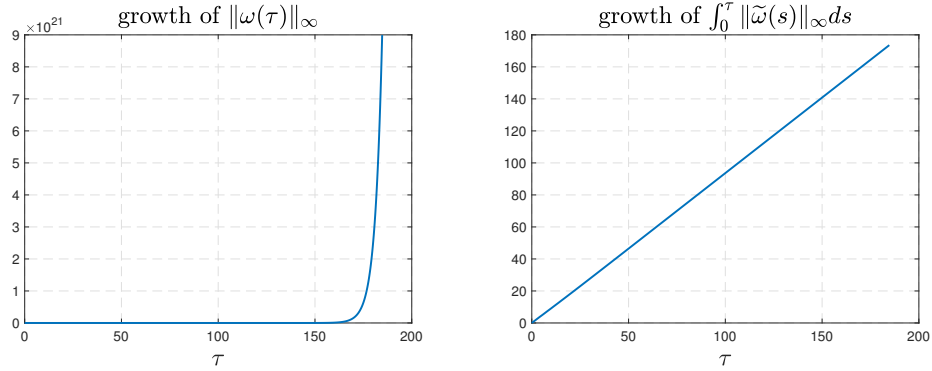


Figure 4.1: Left plot: Dynamic growth of the maximum vorticity as a function of τ . Right plot: The growth of $\int_0^\tau \|\tilde{\omega}\|_{L^\infty} ds$ as a function of τ . The perfect linear fitting implies that $\|\omega(t)\|_{L^\infty} = O\left(\frac{1}{T-t}\right)$.

In Figure 4.1(a), we plot the dynamic growth of the maximum vorticity as a function of τ . We observe a rapid growth of $\|\omega\|_\infty$. By the end of the computation, the maximum vorticity has increased by a factor of 9×10^{21} . To best of our knowledge, such a large growth rate of the maximum vorticity has not been reported for the 3D Euler or Navier–Stokes equations in the literature. In Figure 4.1(b), we plot the time integral of the maximum vorticity $\int_0^t \|\omega(s)\|_\infty ds = \int_0^\tau \|\tilde{\omega}(s')\|_\infty ds'$. We observe a perfect linear growth of the time integral of the maximum vorticity with respect to τ . Since $\tau = c_0 |\log(T-t)|$, this implies that $\|\omega\|_\infty \sim \frac{1}{T-t}$. This violates the Beale-Kato-Majda blowup criterion [1]

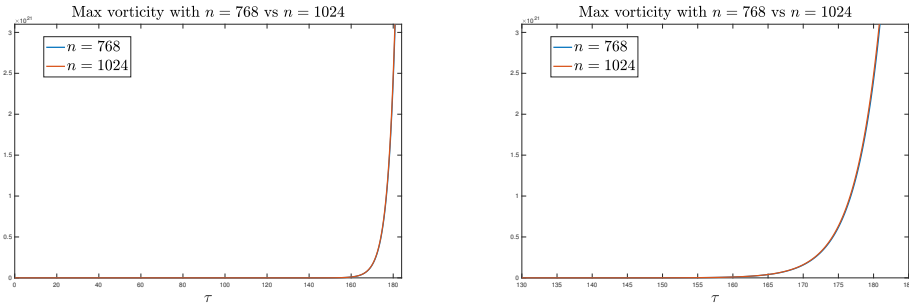


Figure 4.2: Left plot: Comparison of $\|\omega(\tau)\|_{L^\infty}/\|\omega(0)\|_{L^\infty}$ in time, $n = 768$ (blue) vs $n = 1024$ (red). Right plot: Zoomed-in version.

In Figure 4.2 (a), we compare the growth rate of the maximum vorticity using two different resolutions, 768×768 vs 1024×1024 . A zoomed-in version is provided in Figure 4.2 (b). We can see that the maximum vorticity computed by the resolution 1024×1024 grows slightly faster than that computed by the resolution 768×768 . This indicates that the higher resolution captures the growth of the maximum vorticity more accurately, but their difference is very small, indicating that the solution is well resolved by the 1024×1024 grid.

In Figure 4.3, we present the 3D solution profiles of $(\tilde{u}_1, \tilde{\omega}_1, \tilde{\Gamma}, \tilde{\psi}_{1,\eta})$ at time $\tau = 185$. By this time, the maximum vorticity has increased by a factor of 9×10^{21} as we can see from Figure 4.1. We observe that the singular support of the profiles travels toward the origin with distance of order $O(10^{-15})$. Note that the position (R, Z) where u_1 achieves its maximum has been fixed to be at $(R_0, 1)$. Due to the viscous regularization, the profile of \tilde{u}_1 remains relatively smooth near (R, Z) . Moreover, the thin structure for ω_1 that we observed for the 3D Euler equations in [35] becomes much smoother. The tail part of u_1 and ω_1 is quite smooth and decays rapidly into the far field.

Due to the relatively small viscosity ν for $\tilde{\Gamma}$, we observe that the total circulation $\tilde{\Gamma}$ develops a traveling wave with a relatively sharp front, propagating toward the origin. The diffusion term in the $\tilde{\omega}_1$ equation regularizes the nearly singular source term due to the sharp traveling wave profile of $\tilde{\Gamma}$ and generates a regularized Delta function like profile for $\tilde{\omega}_1$. We observe that $\tilde{\psi}_{1,\eta}$ achieves its maximum value at $\eta = 0$ near $\xi = R_0$. This property is crucial in generating a traveling wave that propagates toward $\eta = 0$, overcoming the destabilizing effect of the transport along the η direction.

We observe that the rescaled profile $\tilde{\omega}_1$ decays rapidly in the far field with boundary values of $O(10^{-18})$. Similar observation also applies to u_1 whose boundary values are of order $O(10^{-12})$. The rescaled profile $\tilde{\psi}_1$ also has a fast decay in the far field with boundary values of order $O(10^{-6})$. On the other hand, a portion of $\tilde{\Gamma}$ in the near field is transported to the far field, resulting in $O(1)$ values of $\tilde{\Gamma}$ in the far field. We note that $\tilde{\Gamma}$ contributes to the generalized Navier–Stokes equations only through the vortex stretching term $(\tilde{\Gamma}^2/\xi^4)_\eta$, which is extremely small with order $O(10^{-34})$ at the far field boundary. Therefore, we do not need to enforce the decay of $\tilde{\Gamma}$ in the far field. Moreover, the boundary values of the transport terms for $\tilde{\Gamma}$ and $\tilde{\omega}_1$ are of order 10^{-9} and 10^{-29} , respectively.

4.2. The streamlines. In this subsection, we investigate the features of the velocity field. We first study the velocity field by looking at the induced streamlines. Interestingly the induced streamlines look qualitatively the same as those obtained for the 3D Navier–Stokes equations in a periodic cylinder [36]. In Figure 4.4, we plot the streamlines induced by the velocity field $\tilde{\mathbf{u}}$ at $\tau = 185$ for different initial points. By this time, the ratio between the maximum vorticity and the initial maximum vorticity, i.e. $\|\boldsymbol{\omega}(t)\|_{L^\infty}/\|\boldsymbol{\omega}(0)\|_{L^\infty}$, has increased by a factor of 9×10^{21} .

The velocity field resembles that of a tornado spinning around the symmetry axis (the green pole). In Figure 4.4(a) with $(r_0, z_0) = (4, 1.5)$, we observe that the streamlines form a torus spinning around the symmetry axis. In Figure 4.4(b) with $(r_0, z_0) = (2, 0.25)$, the streamlines go straight upward without any spinning. In Figure 4.4(c) with $(r_0, z_0) = (6, 2.5)$, the streamlines first go downward, then travel inward and upward, finally travel downward and spin outward. In Figure 4.4(d) with $(r_0, z_0) = (6, 2)$, the streamlines first spin downward and then outward. The solution behaves qualitatively the same as what we observed for the axisymmetric Navier–Stokes equations in a periodic cylinder [36].

4.3. The 2D flow. To understand the phenomena in the most singular region as shown in Figure 4.4, we study the 2D velocity field (u^r, u^z) . In Figure 4.5(a)-(b), we plot the dipole structure of $\tilde{\omega}_1$ in a local symmetric region and the hyperbolic velocity field induced by the dipole structure in a local microscopic domain $[0, R_b] \times [0, Z_b]$ at $\tau = 185$. The dipole structure for the generalized Navier–Stokes equations look qualitatively similar to that of the 3D Navier–Stokes equations in a periodic cylinder [36]. As in the case of the 3D Navier–Stokes equations in a periodic cylinder, the negative radial velocity near

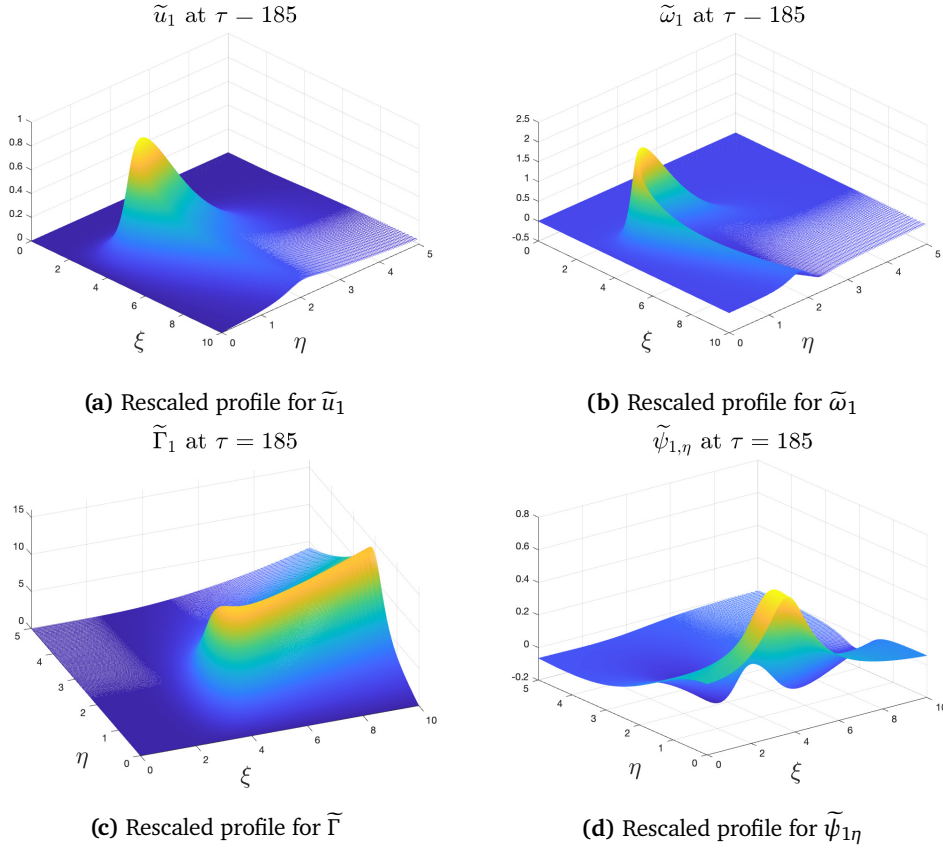


Figure 4.3: The local view of rescaled profiles at time $\tau = 185$. (a) \tilde{u}_1 ; (b) $\tilde{\omega}_1$; (c) $\tilde{\Gamma}$; (d) $\tilde{\psi}_{1,\eta}$.

$\eta = 0$ induced by the antisymmetric vortex dipoles pushes the solution toward $\xi = 0$, then move upward away from $\eta = 0$. This is one of the driving mechanisms for a potential singularity on the symmetry axis. Since the value of \tilde{u}_1 becomes very small near the symmetry axis $\xi = 0$, the streamlines almost do not spin around the symmetry axis, as illustrated in Figure 4.4(b).

We also observe that the velocity field $(u^r(t), u^z(t))$ forms a closed circle right above (R, Z) . The corresponding streamlines are trapped in the circle region in the $\xi\eta$ -plane, which is responsible for the formation of the spinning torus that we observed earlier in Figure 4.4(a).

We can also understand this hyperbolic flow structure from the velocity contours in Figure 4.6 (a)-(b). As we can see from Figure 4.6(a), the radial velocity u^r is negative and large in amplitude below the red dot (R, Z) where \tilde{u}_1 achieves its maximum, pushing the flow toward the symmetry axis $\xi = 0$. But it becomes large and positive above (R, Z) , pushing the flow outward. Similarly, we can see from Figure 4.6(b) that the axial velocity u^z is negative and large in amplitude to the right hand side of (R, Z) , pushing the flow downward toward $\eta = 0$. But it becomes large and positive on the left hand side of (R, Z) , pushing the flow upward away from $\eta = 0$. This is the driving mechanism for forming the hyperbolic flow structure near the origin.

In Figure 4.7(a)-(b), we demonstrate the alignment between $\tilde{\psi}_{1,\eta}$ and \tilde{u}_1 at $\tau = 185$. Although the maximum vorticity has grown a lot by this time, the local solution structures have remained qualitatively the same in the late stage of the computation. This shows that the viscous effect has a strong stabilizing effect that enhances the nonlinear alignment of vortex stretching. We also observe that $\tilde{\psi}_{1,\eta}$ is relatively flat in the region $\{(\xi, \eta) | 0 \leq \xi \leq 0.9R, 0 \leq \eta \leq 0.5Z\}$. This property is critical for \tilde{u}_1 to remain large between the sharp front and $\xi = 0$, thus avoiding developing a two-scale structure.

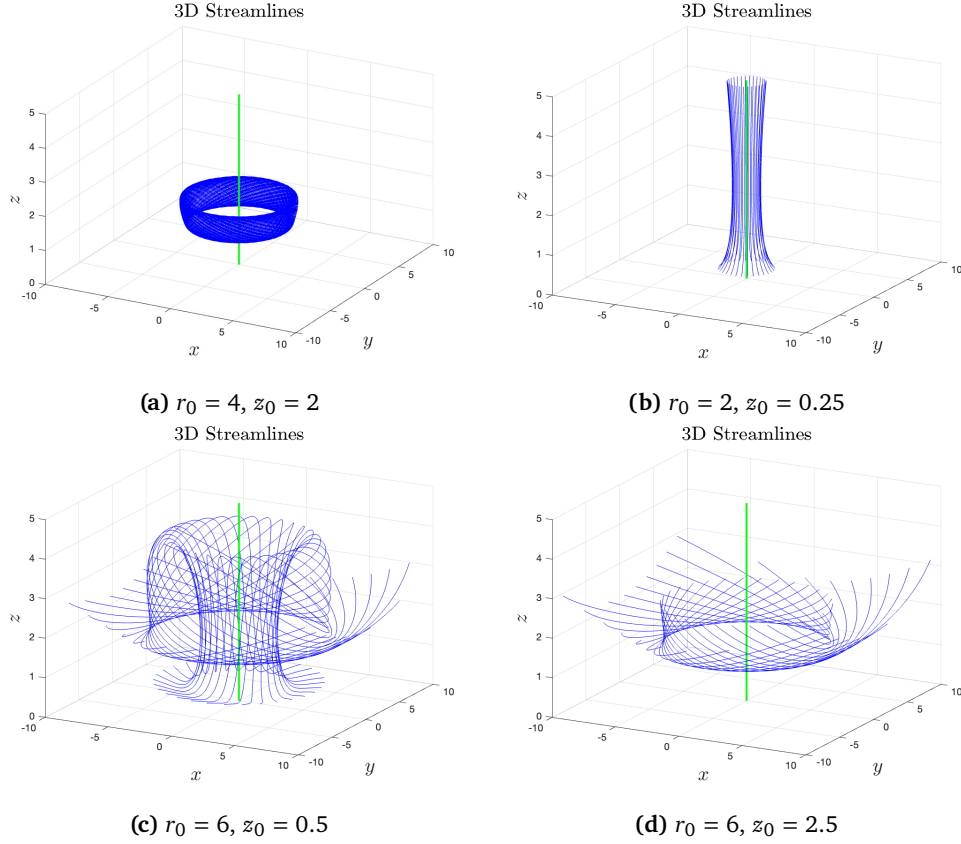


Figure 4.4: The streamlines of $(u^r(t), u^\theta(t), u^z(t))$ at time $\tau = 185$ with initial points given by (a) $(r_0, z_0) = (4, 2)$, streamlines form a torus; (b) $(r_0, z_0) = (2, 0.25)$, streamlines go straight upward; (c) $(r_0, z_0) = (6, 0.5)$, streamlines first go downward, then travel inward, finally go upward; (d) $(r_0, z_0) = (6, 2.5)$, streamlines spin downward and outward. The green pole is the symmetry axis $r = 0$.

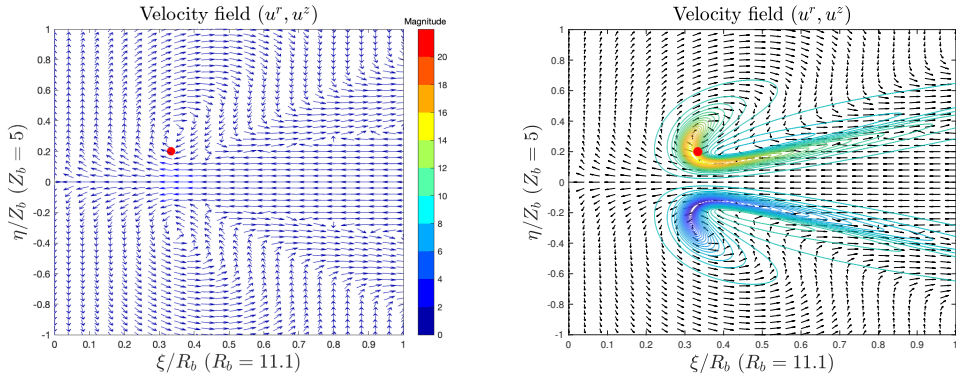


Figure 4.5: The dipole structure of ω_1 and the induced local velocity field at $\tau = 185$. Left plot: the velocity vector. Right plot: the velocity vector with the ω_1 contour as background. The red dot is the position (R, Z) where \tilde{u}_1 achieves its maximum.

We observe that the large, positive, and relative flat $\tilde{\psi}_{1\eta}$ near $\eta = 0$ induces a large growth of \tilde{u}_1 through the vortex stretching term $2\tilde{\psi}_{1\eta}\tilde{u}_1$ in the \tilde{u}_1 -equation (2.1a). We also note that $\tilde{\psi}_{1\eta}$ is positive to the left hand side of $\eta = Z$ and negative to the right hand side of $\eta = Z$. Thus the nonlinear vortex stretching term $\tilde{\psi}_{1\eta}\tilde{u}_1$ generates a traveling wave that pushes the solution toward $\eta = 0$, overcoming

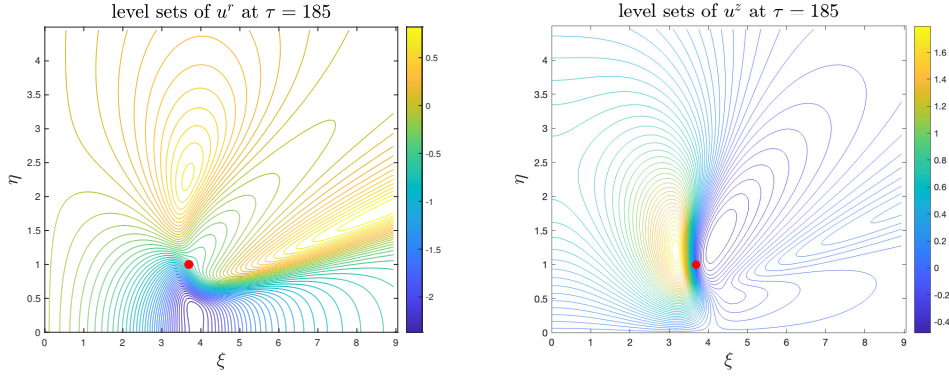


Figure 4.6: The level sets of \tilde{u}^ξ (left) and \tilde{u}^η (right) at $\tau = 185$. The red point is the maximum location (R, Z) of \tilde{u}_1 .

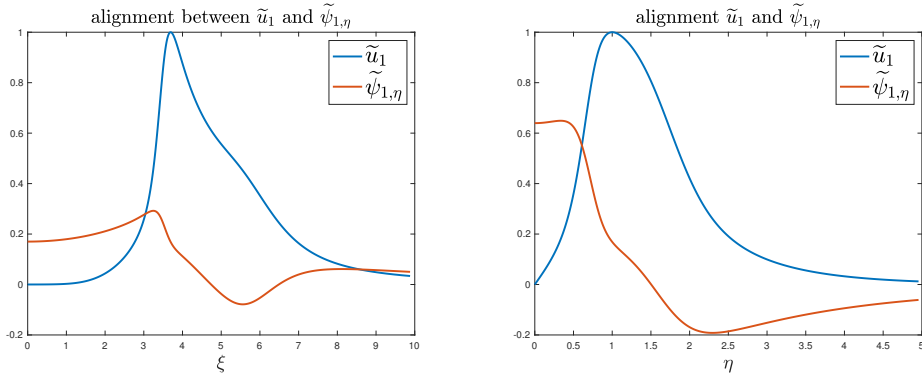


Figure 4.7: Left plot: Alignment between alignment \tilde{u}_1 and $\tilde{\psi}_{1,\eta}$ at $\eta = Z$ as a function of ξ at $\tau = 185$. Right plot: Alignment between alignment \tilde{u}_1 and $\tilde{\psi}_{1,\eta}$ at $\xi = R$ as a function of η at $\tau = 185$.

the destabilizing effect of the transport along the η direction, which tries to push the solution outward away from $\eta = 0$. Due to the oddness of \tilde{u}_1 as a function of η , the large growth of u_1 near $\eta = 0$ generates a large positive gradient of \tilde{u}_1^2 in the η -direction between $\eta = 0$ and $\eta = Z$. The vortex stretching term $(\tilde{u}_1^2)_\eta$ in the $\tilde{\omega}_1$ -equation (2.1b) then induces a growth of $\tilde{\omega}_1$. This in turn generates growth of $\tilde{\psi}_{1\eta}$ near $\eta = 0$. The whole coupling mechanism forms a positive feedback loop.

4.4. Alignment of vortex stretching. Due to the viscous regularization, the solution becomes smoother and is more stable. We are able to compute up to a time when $(R(t), Z(t))$ is very close to the origin. This is something we could not achieve for the 3D Navier–Stokes equations in a periodic cylinder [36]. In Figure 4.8(a), we observe that the positive alignment between \tilde{u}_1 and $\tilde{\psi}_{1\eta}$ converges to a constant as τ increases. This indicates that the generalized Navier–Stokes equations with solution dependent viscosity achieves a self-similar scaling relationship. We observe some mild oscillations in time for the alignment and the normalized coefficients in Figure 4.8. This is due to the rapid decay of the solution dependent viscosity $\nu(t)$ in time (see Figure 4.9(b)), which is not strong enough to stabilize the shearing instability induced by the sharp front of Γ in the generalized Euler equations.

In the Figure 4.8(b), we plot the normalized scaling parameters $\hat{c}_{l_z} = c_{l_z}/(c_{l_z} - c_\psi)$ and $\hat{c}_{l_r} = c_{l_r}/(c_{l_z} - c_\psi)$. We observe that they converge to the same constant $c_l = 0.523$ as τ increases. This shows that $R(t)$ and $Z(t)$ have the same scale. Since $\|u_1\|_\infty = 1/(T - t)$ and $Z(t) = (T - t)^{c_l}$, the solution dependent viscosity is given by $\nu = \nu_0 \|u_1(\tau)\|_\infty Z(t)^2 = \nu_0 (T - t)^{2c_l - 1} = \nu_0 (T - t)^{0.1272}$.

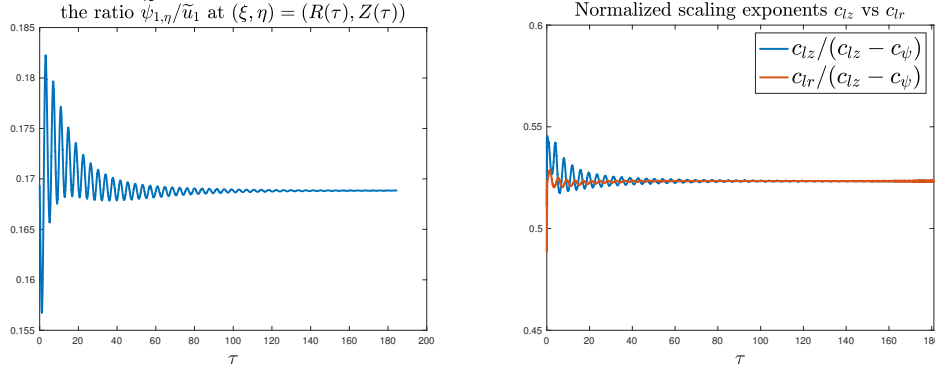


Figure 4.8: Left plot: The ratio between $\tilde{\psi}_{1,\eta}$ and \tilde{u}_1 at $(\xi, \eta) = (R, Z)$ as a function of τ . Right plot: The normalized scaling exponent $c_{lz}/(c_{lz} - c_\psi)$ and $c_{lr}/(c_{lz} - c_\psi)$ as a function of τ .

4.5. Balance between vortex stretching and diffusion and self-similar profile. In this subsection, we study the balance between the vortex stretching terms and the diffusion terms for both \tilde{u}_1 and $\tilde{\omega}_1$ equations. Using the scaling relationship $c_u = c_\psi - c_{lz}$ given by (3.1), we can easily show that the solution dependent viscosity satisfies

$$\nu(\tau) = \nu_0 \|u_1\|_\infty Z(t)^2 = \nu_0 C_{lz}/C_\psi,$$

which exactly cancels the scaling factor C_ψ/C_{lz} in front of the rescaled diffusion term. This is why we obtain constant viscosity ν_0 in the dynamic rescaling formulation for both \tilde{u}_1 and $\tilde{\omega}_1$ equations.

In Figure 4.9(a), we plot the ratio between the vortex stretching term $2\tilde{\psi}_{1,\eta}\tilde{u}_1$ and the diffusion term $-\nu_0\Delta\tilde{u}_1$ at (R, Z) where \tilde{u}_1 achieves its maximum. We observe that this ratio converges to a constant value 5.22 as τ increases. This shows that the vortex stretching term dominates the diffusion term. In the same figure, we also plot the ratio between $(\tilde{u}_1^2)_\eta$ and $-\nu_0\Delta\tilde{\omega}_1$ at (R_ω, Z_ω) where $\tilde{\omega}_1$ achieves its maximum. We do not include the contribution from the term $(n-3)\tilde{\psi}_{1,\eta}\tilde{\omega}_1$ since $(n-3)\tilde{\psi}_{1,\eta}\tilde{\omega}_1$ is only 7% of $(\tilde{u}_1^2)_\eta$ at (R_ω, Z_ω) . We observe that the ratio of these two terms converges to a constant value 2.4 as τ increases, which again shows that the vortex stretching term dominates the diffusion, but the diffusion term has a nontrivial contribution as the solution develops a self-similar blowup. The balance between the vortex stretching terms and the diffusion terms is crucial in maintaining the robust nonlinear growth of the maximum vorticity in time.

In Figure 4.9(b), we plot the solution dependent viscosity $\nu(\tau) = \nu_0 \|u_1\|_\infty Z(\tau)^2$ as a function of τ . We observe that this solution dependent viscosity decays to zero as τ increases with $\nu(185) = 1.3 \cdot 10^{-6}$.

In Figure 4.10(a), we plot the ratio between $Z(\tau)$ and $R(\tau)$. We observe that the ratio $Z(\tau)/R(\tau)$ converges to a constant value of 0.914. This shows that we have an one-scale blowup. In Figure 4.10(b), we plot the space dimension $n(\tau) = 1 + 2R(\tau)/Z(\tau)$ as a function of τ . We observe that the space dimension is relatively flat and seems to settle down to a constant value $n = 3.188$ by $\tau = 185$.

In Figure 4.11, we plot the contours of \tilde{u}_1 and $\tilde{\omega}_1$ as a function of (ξ, η) for three different time instants, $\tau = 159, 172, 185$ using resolution 1024×1024 . During this time interval, the maximum vorticity has increased by a factor of 1029. We observe that these contours are almost indistinguishable from each other. This shows that u_1 and ω_1 develop a self-similar blowup with scaling proportional to $C_{lz} \sim (T-t)^{c_l}$ and $C_{lr} \sim (T-t)^{c_l}$ ($c_l = 0.523$).

5. BLOWUP OF THE GENERALIZED BOUSSINESQ SYSTEM WITH CONSTANT VISCOSITY

In this section, we will investigate the nearly self-similar blowup of the generalized Boussinesq system with two constant viscosity coefficients. If we choose the two viscosity coefficients to be the

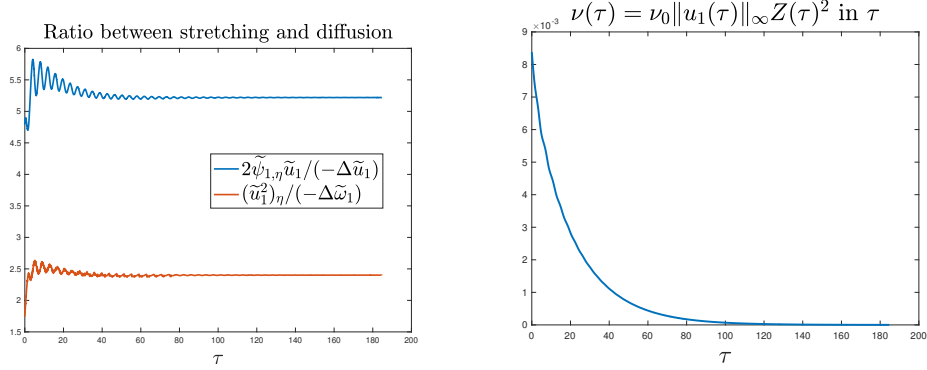


Figure 4.9: Left plot: Ratio between the vortex stretching term $2\tilde{\psi}_{1,\eta}\tilde{u}_1$ and the diffusion term $-\nu_0\Delta\tilde{u}_1$ at (R, Z) (blue) and ratio between the vortex stretching term $(\tilde{u}_1^2)_\eta$ and the diffusion term $-\nu_0\Delta\tilde{\omega}_1$ at (R_ω, Z_ω) (red) in τ . Right plot: Viscosity $\nu(\tau) = \nu_0\|u_1(\tau)\|_\infty Z(\tau)^2$ in τ with $\nu(185) = 1.3 \cdot 10^{-6}$.

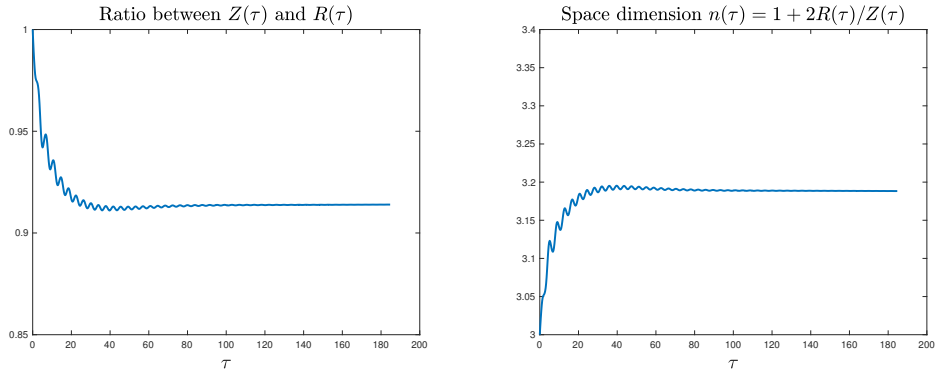


Figure 4.10: Left plot: Ratio of $Z(\tau)/R(\tau)$ as a function of τ . Right plot: The space dimension $n(\tau) = 1 + 2R(\tau)/Z(\tau)$ as a function of τ with $n(185) = 3.188$.

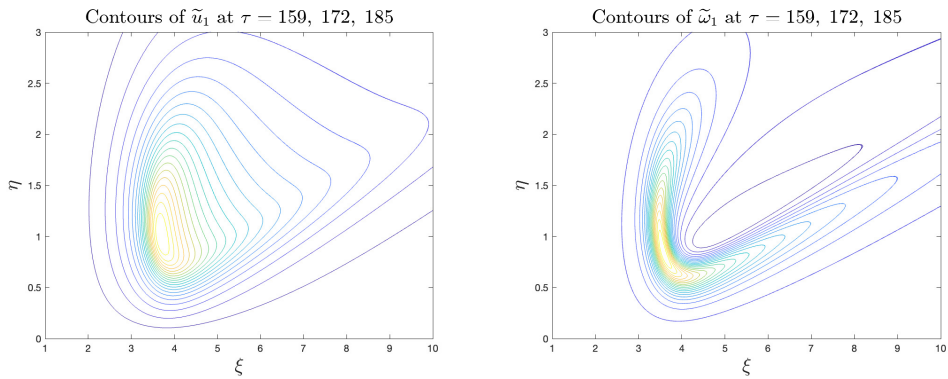


Figure 4.11: Left plot: Contours of \tilde{u}_1 with respect to (ξ, η) . Right plot: Contours of $\tilde{\omega}_1$ with respect to (ξ, η) at $\tau = 159, 172, 185$ during which the maximum vorticity has grown by a factor of 1029.

same constant viscosity ν_0 , we find that the solution of the generalized Boussinesq system either develops a turbulent flow if ν_0 is too small or becomes a laminar flow if ν_0 is too large. After performing many experiments, we find that $\nu_1 = 6 \cdot 10^{-4}$ and $\nu_2 = 6 \cdot 10^{-3}$ seem to give robust one-scale nearly self-similar blowup. This choice of viscosity coefficients produces a stable nonlinear alignment of vortex

stretching and nearly self-similar scaling properties. We choose a stronger cut-off function to cut off the far field tail of the solution obtained by solving the 3D Navier–Stokes using an adaptive mesh. The modified initial data behave like a pair of anti-symmetric vortex rings circled around the symmetry axis.

5.1. Rapid growth of maximum vorticity. In this subsection, we investigate how the profiles of the solution evolve in time. We will use the numerical results computed on the adaptive mesh of resolution $(n_1, n_2) = (1024, 1024)$. We have computed the numerical solution up to time $\tau = 155$ when it is still well resolved.

In Figure 5.1, we present the solution profiles of $(\tilde{u}_1, \tilde{\omega}_1, \tilde{\Gamma}, \tilde{\psi}_{1,\eta})$ at time $\tau = 155$. By this time, the maximum vorticity has increased by a factor of $1.4 \cdot 10^{30}$. We observe that the singular support of the profiles travels toward the origin with distance of order $O(10^{-15})$.

The solution profiles look qualitatively similar to those for the generalized Navier–Stokes equations with solution dependent viscosity. Due to the relatively small viscosity ν_1 for $\tilde{\Gamma}$, we observe that the density $\tilde{\Gamma}$ forms a shock like traveling wave profile, propagating toward the symmetry axis $\xi = 0$. This sharp shock like profile induces a Delta function like source term for the $\tilde{\omega}_1$ equation. The relatively large viscosity ν_2 then regularizes this nearly singular source term and generates a regularized Delta function like profile for $\tilde{\omega}_1$. We observe that $\tilde{\psi}_{1,\eta}$ achieves its maximum value at $\eta = 0$ near $\xi = R_0$. As we commented earlier, this is a crucial property that overcomes the destabilizing effect of the transport along the η direction, which pushes the solution upward away from $\eta = 0$.

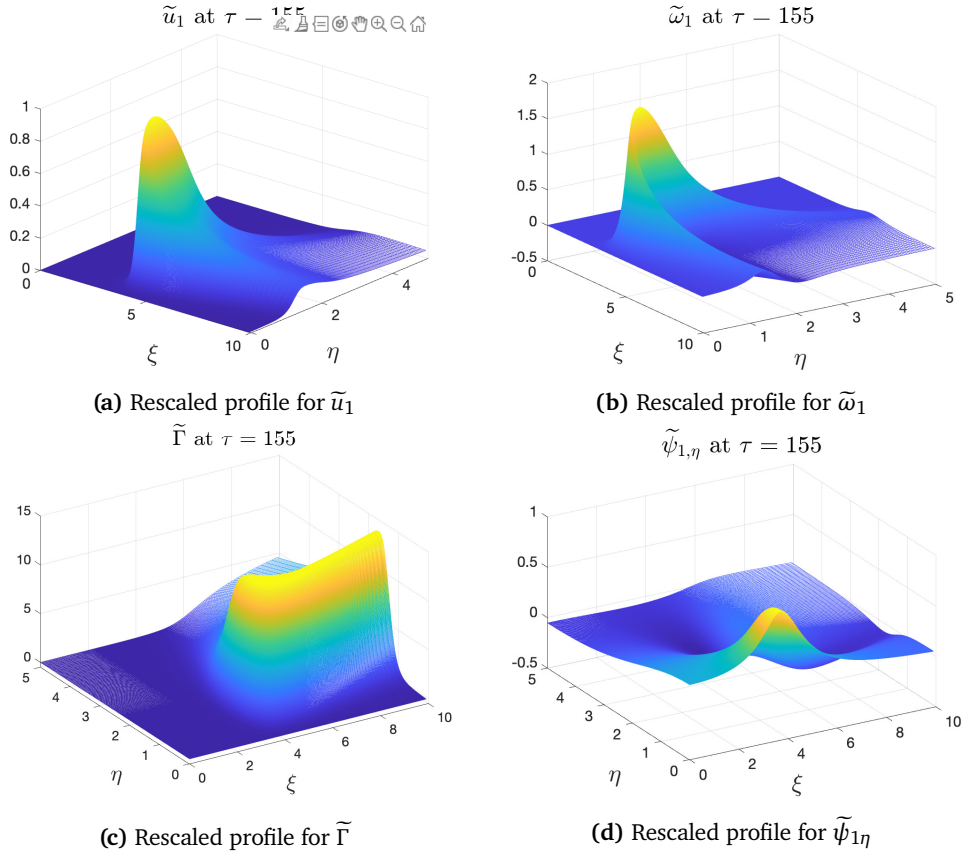


Figure 5.1: The local view of rescaled profiles at time $\tau = 155$. (a) \tilde{u}_1 ; (b) $\tilde{\omega}_1$; (c) $\tilde{\Gamma}$; (d) $\tilde{\psi}_{1,\eta}$.

We observe that the rescaled profile $\tilde{\omega}_1$ decays rapidly in the far field with boundary values of $O(10^{-21})$. The rescaled profile $\tilde{\psi}_1$ also has a fast decay in the far field with boundary values of order

$O(10^{-8})$. Although the boundary values of $\tilde{\Gamma}$ are $O(1)$, the vortex stretching term $(\tilde{\Gamma}^2/\xi^4)_\eta$ is extremely small at the far field boundary of order $O(10^{-35})$. Moreover, the boundary values of the transport terms for $\tilde{\Gamma}$ and $\tilde{\omega}_1$ are of order $O(10^{-13})$ and $O(10^{-34})$, respectively.

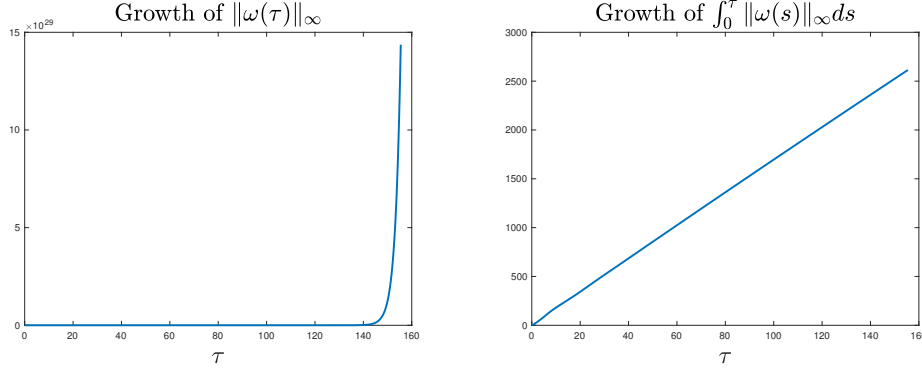


Figure 5.2: Left plot: the amplification of maximum vorticity relative to its initial maximum vorticity, $\|\omega(\tau)\|_{L^\infty}/\|\omega(0)\|_{L^\infty}$ as a function of time. Right plot: the time integral of maximum vorticity, $\|\tilde{\omega}(0)\|_{L^\infty}^{-1} \int_0^\tau \|\tilde{\omega}(s)\|_{L^\infty} ds$ as a function of time. The solution is computed using 1024×1024 grid. The final time instant is $\tau = 155$.

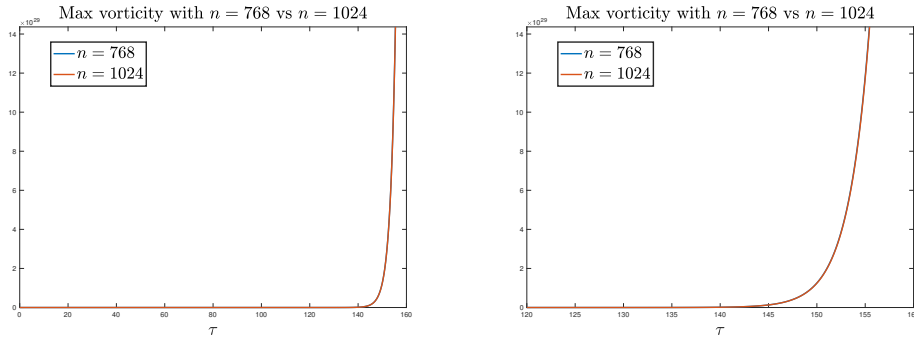


Figure 5.3: Left plot: Comparison of $\|\omega(\tau)\|_{L^\infty}/\|\omega(0)\|_{L^\infty}$ in time, $n = 768$ (blue) vs $n = 1024$ (red). Right plot: Zoomed-in version.

We observe that the solution develops rapid growth dynamically. In the left subplot of Figure 5.2, we compute the relative growth of the maximum vorticity $\|\omega(t)\|_{L^\infty}/\|\omega(0)\|_{L^\infty}$ as a function of τ . We can see that the maximum vorticity grows extremely rapidly in time. We observe that $\|\omega(t)\|_{L^\infty}/\|\omega(0)\|_{L^\infty}$ has increased by a factor of $1.4 \cdot 10^{30}$ by the end of the computation. To best of our knowledge, such a large growth rate of the maximum vorticity has not been reported for the 3D incompressible Navier–Stokes equations in the literature.

In the right subplot of Figure 5.2, we plot that the time integral of the maximum vorticity in the rescaled time τ , i.e. $\int_0^\tau \|\tilde{\omega}(s)\|_{L^\infty} ds$ as a function of τ . We observe that the growth rate is roughly linear with respect to τ . This implies that the growth rate of the maximum vorticity is proportional $O(\frac{1}{T-t})$. The rapid growth of $\int_0^t \|\omega(s)\|_{L^\infty} ds$ violates the well-known Beale-Kato-Majda blow-up criterion [1], which implies that the generalized axisymmetric Navier–Stokes equations develop a finite time singularity.

In Figure 5.3 (a), we compare the growth rate of the maximum vorticity using two different resolutions, 768×768 vs 1024×1024 . A zoomed-in version is provided in Figure 5.3 (b). We can see

that the two curves are almost indistinguishable with the 1024×1024 resolution gives a slightly faster growth. This indicates that the maximum vorticity is well resolved by our computational mesh.

5.2. Alignment of vortex stretching. Due to the viscous regularization, the solution becomes smoother and is more stable. We are able to compute up to a time when $(R(t), Z(t))$ is very close to the origin with distance of order $O(10^{-15})$. This is something we could not achieve for the 3D Navier–Stokes equations in a periodic cylinder [36].

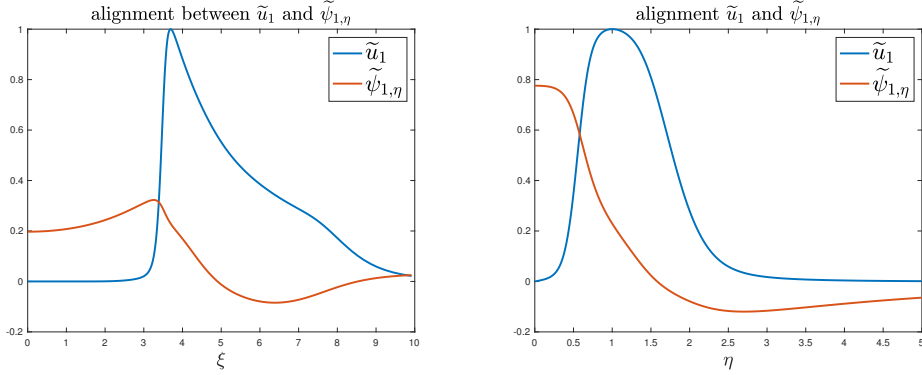


Figure 5.4: Left plot: Alignment between \tilde{u}_1 and $\tilde{\psi}_{1,\eta}$ at $\eta = Z$ as a function of ξ at $\tau = 155$. We observe a sharper front along the ξ direction due to the fact that we use a smaller viscosity ν_1 . Right plot: Alignment between \tilde{u}_1 and $\tilde{\psi}_{1,\eta}$ at $\xi = R$ as a function of η at $\tau = 155$.

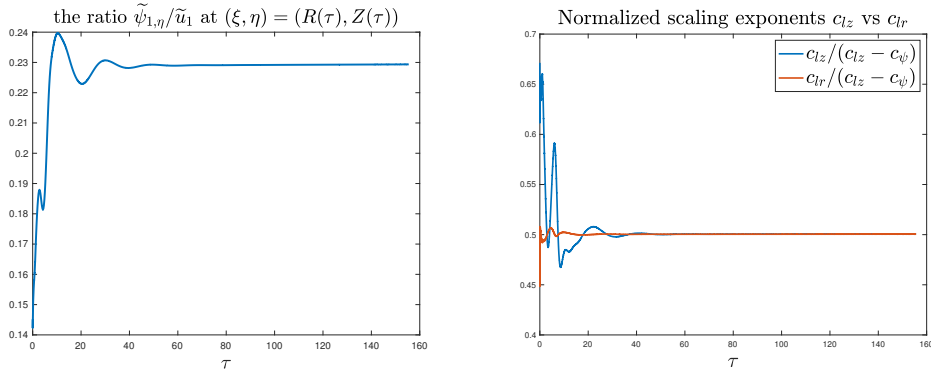


Figure 5.5: Left plot: The ratio between $\tilde{\psi}_{1,\eta}$ and \tilde{u}_1 at $(\xi, \eta) = (R, Z)$ as a function of τ . Right plot: The normalized scaling exponent $c_{lz}/(c_{lz} - c_\psi)$ and $c_{lr}/(c_{lz} - c_\psi)$ as a function of τ .

In Figure 5.4(a)-(b), we demonstrate the alignment between $\tilde{\psi}_{1,\eta}$ and \tilde{u}_1 at $\tau = 155$. Although the maximum vorticity has grown so much by this time, the local solution structures have remained qualitatively the same in the late stage of the computation. We observe that the viscous effect actually enhances the nonlinear alignment of vortex stretching. Although we use two constant viscosity coefficients here, we observe qualitatively the same phenomena as we did for the generalized Navier–Stokes equations with solution dependent viscosity. In particular, $\tilde{\psi}_{1,\eta}$ is relatively flat in a local region near the origin. This is an essential property that prevents the formation of a two-scale structure. Moreover, we observe the same qualitative positive feedback mechanism as we observed for the generalized Navier–Stokes equations with solution dependent viscosity.

In Figure 5.5(a), we observe that the positive alignment between \tilde{u}_1 and $\tilde{\psi}_{1\eta}$ is almost flat in time with a mild increase in the late stage of the computation. This indicates that the generalized axisymmetric Boussinesq system achieves a nearly self-similar scaling relationship.

In the Figure 5.5 (b), we plot the normalized scaling exponents $c_{l_z}/(c_{l_z} - c_\psi)$ and $c_{l_r}/(c_{l_z} - c_\psi)$ as a function of τ . We observe that they both seem to approach 0.5 as τ increases. On the other hand, due to the numerical dissipation introduced by the numerical interpolation from the old mesh to the new mesh for the expanding domain and the first order accuracy of the splitting scheme, we observe that the convergence to 0.5 saturates in the late stage. We remark that we have solved the dynamic rescaling formulation for 2.65 millions time steps with an increasingly coarser mesh in the near field since we need to allocate more grid points to the far field to cover the expanding computational domain. Thus, numerical errors will inevitably increase in a long time computation, which will affect our ability to resolve the scaling exponents accurately for a long time computation.

5.2.1. *The streamlines.* In this subsection, we investigate the features of the velocity field. We first study the velocity field by looking at the induced streamlines. In Figure 5.6, we plot the streamlines induced by the velocity field $\mathbf{u}(t)$ at $\tau = 155$. By this time, the ratio between the maximum vorticity and the initial maximum vorticity, i.e. $\|\omega(t)\|_{L^\infty}/\|\omega(0)\|_{L^\infty}$, has increased by a factor of $1.4 \cdot 10^{30}$.

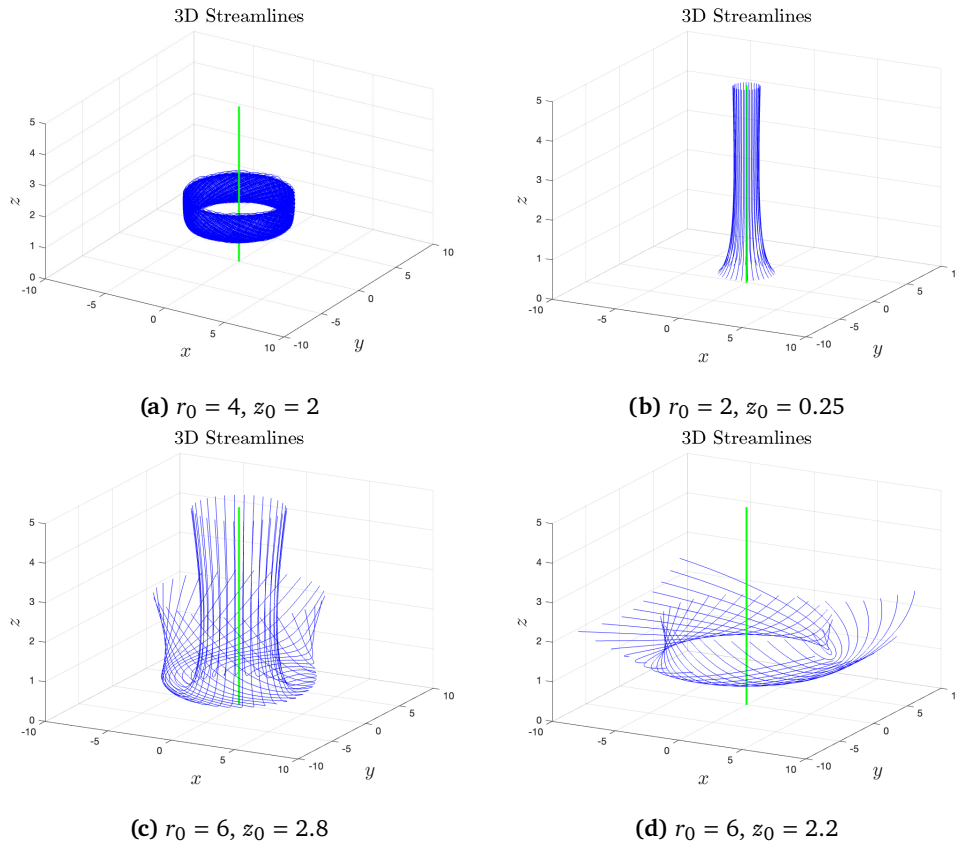


Figure 5.6: The streamlines of $(u^r(t), u^\theta(t), u^z(t))$ at time $\tau = 155$ with initial points given by (a) $(r_0, z_0) = (4, 2)$, streamlines form a torus; (b) $(r_0, z_0) = (2, 0.25)$, streamlines go straight upward; (c) $(r_0, z_0) = (6, 2.8)$, streamlines first go downward, then travel inward, finally go upward; (d) $(r_0, z_0) = (6, 2.2)$, streamlines spin downward and outward. The green pole is the symmetry axis.

Surprisingly the induced streamlines look qualitatively the same as those obtained for the generalized Navier–Stokes equations with solution dependent viscosity. We will use a similar set of parameters

to draw the streamlines to compare with the streamlines obtained for the generalized Navier–Stokes equations that we reported in the previous section. In Figure 5.6(a) with $(r_0, z_0) = (4, 1.5)$, we observe that the streamlines form the same type of torus spinning around the symmetry axis. In Figure 5.6(b) with $(r_0, z_0) = (2, 0.25)$, we observe that the streamlines go straight upward without any spinning. In Figure 5.6(c) with $(r_0, z_0) = (6, 2.8)$, the streamlines first go downward, then travel inward and finally go upward. Note that this starting point is different from the corresponding case for the generalized Navier–Stokes equations with solution dependent viscosity where we used $(r_0, z_0) = (6, 0.5)$. This explains why the two sets of streamlines look different. Finally, we plot in Figure 5.6(d) the streamlines that start with $(r_0, z_0) = (6, 2)$. We can see that the streamlines first spin downward and then outward. It is also interesting to note that the solution behaves qualitatively the same as what we observed for the 3D axisymmetric Navier–Stokes equations in a periodic cylinder [36].

5.2.2. *The 2D flow.* To understand the phenomena in the most singular region as shown in Figure 5.6, we also study the 2D velocity field (u^r, u^z) . In Figure 5.7(a)-(b), we plot the dipole structure of $\tilde{\omega}_1$ in a local symmetric region and the hyperbolic velocity field induced by the dipole structure in a local microscopic domain $[0, R_b] \times [0, Z_b]$ at $\tau = 155$. The dipole structure for the generalized Boussinesq equations with constant viscosity looks qualitatively similar to that of the generalized Navier–Stokes equations with solution dependent viscosity. The negative radial velocity near $\eta = 0$ induced by the vortex dipole pushes the solution toward $\xi = 0$, then move upward away from $\eta = 0$. This is the main driving mechanism for the flow to develop a hyperbolic structure. Since the value of \tilde{u}_1 becomes very small near the symmetry axis $\xi = 0$, the streamlines almost do not spin around the symmetry axis, as illustrated in Figure 5.6(b).

We can also understand this hyperbolic flow structure from the velocity contours in Figure 5.8 (a)-(b). Although the velocity contours look qualitatively the same as those for the generalized Navier–Stokes equations with solution dependent viscosity, a closer look shows that there are some subtle differences in the local solution structure, especially in the shape of vorticity contours of $\tilde{\omega}_1$ if we compare Figure 4.5(b) with Figure 5.7(b). From Figure 5.8(a), we observe that the radial velocity u^r is negative and large in amplitude below the red dot (R, Z) , which pushes the flow toward the symmetry axis $\xi = 0$. The axial velocity u^z is negative and large in amplitude to the right hand side of (R, Z) , pushing the flow downward toward $\eta = 0$. On the left hand side of (R, Z) , it becomes large and positive on the left hand side of (R, Z) , which pushes the flow upward away from $\eta = 0$. This is very similar to the flow structure of the generalized Navier–Stokes equations with solution dependent viscosity.

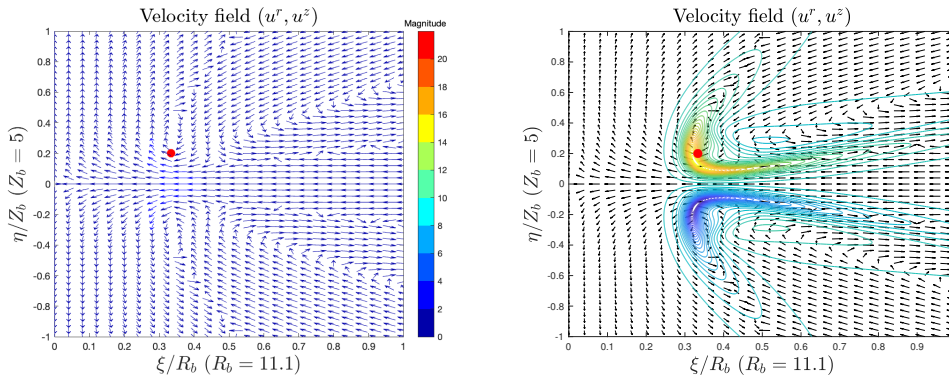


Figure 5.7: The dipole structure of ω_1 and the induced local velocity field at $\tau = 155$. Left plot: the velocity vector. Right plot: the velocity vector with the ω_1 contour as background. The red dot is the position (R, Z) where \tilde{u}_1 achieves its maximum.

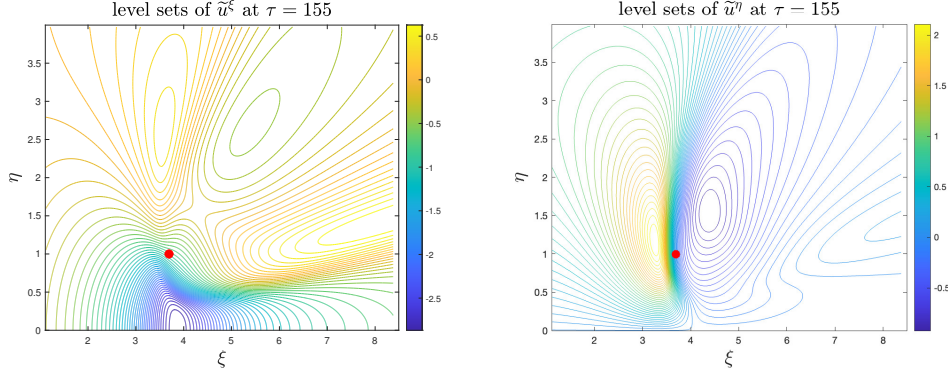


Figure 5.8: The level sets of \tilde{u}^ξ (left) and \tilde{u}^η (right) at $\tau = 155$. The red point is the maximum location (R, Z) of \tilde{u}_1 .

As in the case of the axisymmetric Navier-Stokes equations in a periodic cylinder, the velocity field $(u^r(t), u^z(t))$ forms a closed circle right above (R, Z) . The corresponding streamlines are trapped in the circle region in the $\xi\eta$ -plane, which is responsible for the formation of the spinning torus that we observed earlier.

5.3. Scaling properties of the nearly self-similar blowup. In this subsection, we study the blowup scaling properties. We observe that all the scaling parameters c_{lz} , c_{lr} , c_ψ , c_ω , and c_ψ all converge to a constant value as τ increases. By the discussion in Section 2, we know that we should study the normalized scaling parameters defined by $c_{lz}/(c_{lz} - c_\psi)$, $c_{lr}/(c_{lz} - c_\psi)$, $c_\psi/(c_{lz} - c_\psi)$, etc. In Figure 5.9 (a), we plot the space dimension $n(\tau) = 3 + 4(R(\tau)/Z(\tau) - 1)$ as a function of τ . As we can see, $n(\tau)$ remains relatively flat in the late stage with $n(155) = 4.73$. In Figure 5.9(b), we plot $C_\psi(\tau)/C_{lz}(\tau)$ as a function of τ . We observe that $C_\psi(\tau)/C_{lz}(\tau)$ roughly has a linear growth with respect to τ with a very small slope ϵ since the growth of $C_\psi(\tau)/C_{lz}(\tau)$ is very small over a long time.

From the discussion in Section 2, we know that

$$\tau = c_0 \log\left(\frac{1}{T-t}\right), \quad C_{lz} = (T-t)^{\widehat{c}_{lz}}, \quad C_\psi = (T-t)^{1-\widehat{c}_{lz}}.$$

If we assume that

$$C_\psi(\tau)/C_{lz}(\tau) = 1 + \epsilon\tau,$$

for τ large, then we would obtain

$$(T-t)^{1-2\widehat{c}_{lz}} = 1 + \epsilon\tau,$$

which implies

$$\widehat{c}_{lz} = \frac{1}{2} + \frac{\log(1 + \epsilon\tau)}{2\tau}.$$

Thus, we obtain that the convergence of \widehat{c}_{lz} to $1/2$ with a logarithmic rate only. Moreover, if τ is not large and ϵ is small, we get $\widehat{c}_{lz} \approx 1/2 + \epsilon/2$. By substituting $\widehat{c}_{lz} = \frac{1}{2} + \frac{\log(1+\epsilon\tau)}{2\tau}$ into $C_{lz} = (T-t)^{\widehat{c}_{lz}}$, we further obtain

$$\lambda(t) = \frac{C_{lz}}{\sqrt{T-t}} = \frac{1}{\sqrt{1 + \epsilon\tau}} = \frac{1}{\sqrt{1 + c_0\epsilon|\log(T-t)|}}.$$

Since $\widehat{c}_u = c_u/(c_{lz} - c_\psi) = -1$, we conclude that $C_u \approx (T-t)$ and $\|u_1\|_\infty = O(1/(T-t))$, which implies

$$\|\omega\|_\infty = O\left(\frac{1}{T-t}\right).$$

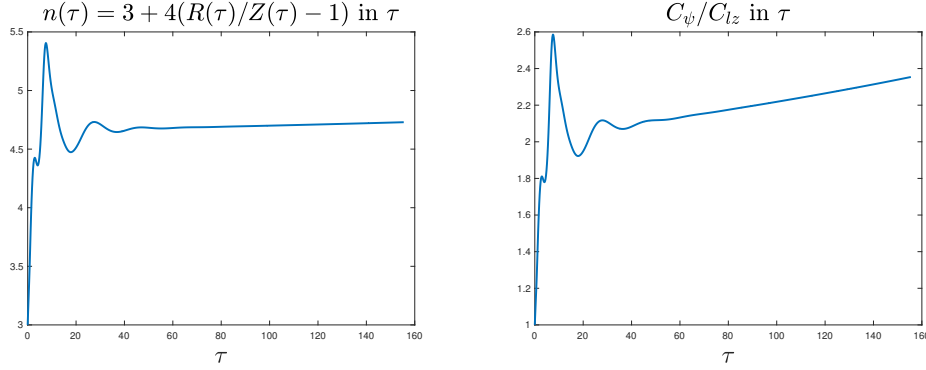


Figure 5.9: Left plot: The space dimension $n(\tau) = 3 + 4(R(\tau)/Z(\tau) - 1)$ as a function of τ with $n(155) = 4.73$. Right plot: C_ψ/C_{l_z} in τ .

5.4. Checking against various blowup criteria. In this subsection, we apply various blowup criteria to confirm the finite time blowup of the generalized Boussinesq system with two constant viscosity coefficients. Our studies show that the nearly self-similar blowup satisfies almost all the generalized blowup criteria that have been established for the 3D axisymmetric Navier–Stokes equations with smooth initial data.

5.4.1. Non-blowup criteria based on enstrophy growth. We first study the growth rate of a generalized enstrophy. For the 3D axisymmetric Navier–Stokes, the enstrophy is defined as $\int |\omega(t)|^2 r dr dz$. In the n -dimensional setting, we define a generalized enstrophy, $\int |\omega(t)|^{n-1} r^{n-2} dr dz$. Using scaling analysis, one can show that if the generalized Boussinesq system develops a self-similar blowup, $\int_0^T \|\omega(t)\|_{L^{n-1}}^q dt$ with $q = \frac{2(n-1)}{n-2}$ will blow up in finite time. Since $\|\omega(t)\|_\infty = O(1/(T-t))$ and C_{l_z} and C_{l_r} scaled like $(T-t)^{1/2}$, we expect that $\|\omega(t)\|_{L^{n-1}}^q$ roughly scales like $(T-t)^{-1}$. In Figure 5.10 (a), we observe that $\|\omega(t)\|_{L^{n-1}}^{n-1}$ develops rapid dynamic growth. In Figure 5.10 (b), we plot $\int_0^T \|\omega(t)\|_{L^{n-1}}^q dt$ as a function of τ . We observe that $\int_0^T \|\omega(t)\|_{L^{n-1}}^q dt$ grows slightly slower than linear growth with respect to τ .

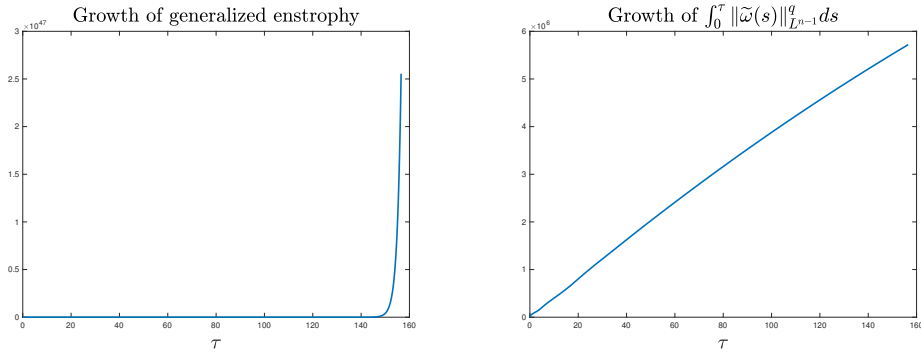


Figure 5.10: Left plot: The dynamic growth of the enstrophy $\int |\omega(t)|^{n-1} r^{n-2} dr dz$ as a function of τ . Right plot: The dynamic growth of $\int_0^\tau \|\tilde{\omega}(s)\|_{L^{n-1}}^q ds$ with $q = \frac{2(n-1)}{n-2}$.

5.4.2. The Ladyzhenskaya-Prodi-Serrin regularity criteria. Next, we study the Ladyzhenskaya-Prodi-Serrin regularity criteria [50, 69, 72], which state that if a Leray-Hopf weak solution \mathbf{u} for the 3D Navier-Stokes equations [56, 34] also lies in $L_t^q L_x^p$, with $3/p + 2/q \leq 1$, then the solution is unique

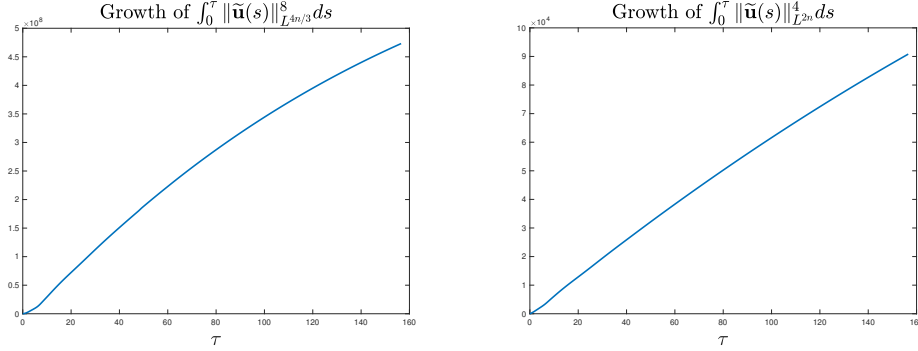


Figure 5.11: Left plot: The dynamic growth of $\int_0^\tau \|\tilde{\mathbf{u}}(s)\|_{L^{4n/3}}^8 ds$ as a function of τ . Right plot: The dynamic growth of $\int_0^\tau \|\tilde{\mathbf{u}}(s)\|_{L^{2n}}^4 ds$ as a function of τ . The nearly linear fitting implies that $\|\mathbf{u}(\tau)\|_{L^{2n,4}} \approx O(\tau^{1/4})$.

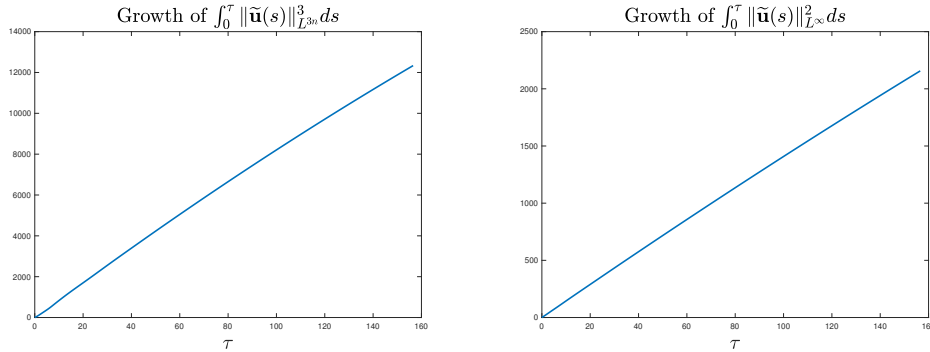


Figure 5.12: Left plot: The dynamic growth of $\int_0^\tau \|\tilde{\mathbf{u}}(s)\|_{L^{3n}}^3 ds$ as a function of τ . The almost linear fitting implies that $\|\mathbf{u}(\tau)\|_{L^{3n,3}} \sim O(\tau^{1/3})$. Right plot: The dynamic growth of $\int_0^\tau \|\tilde{\mathbf{u}}(s)\|_{L^\infty}^2 ds$ as a function of τ . The almost linear fitting implies that $\|\mathbf{u}(\tau)\|_{L^\infty} \sim O(\tau^{1/2})$.

and smooth in positive time. The endpoint result with $p = 3$, $q = \infty$ has been proved in the work of Escauriaza-Seregin-Sverak in [30]. In the n -dimensional setting, one can derive a similar result by studying the $L_t^q L_x^p$ norm of \mathbf{u} with $n/p + 2/q \leq 1$.

In Figure 5.11, we plot the dynamic growth of $\|\mathbf{u}\|_{L^{4n/3,8}}^8$ and $\|\mathbf{u}\|_{L^{2n,4}}^4$. We also plot $\|\mathbf{u}\|_{L^{3n,3}}^3$ in Figure 5.12(a). We can see that they all grow rapidly in time. For larger p with $p = 2n$ and $p = 3n$, the growth rate is almost linear in τ . This suggests that $\|\mathbf{u}\|_{L^{2n,4}} \sim O(\tau^{1/4})$ and $\|\mathbf{u}\|_{L^{3n,3}} \sim O(\tau^{1/3})$.

In Figure 5.12(b), we plot the dynamic growth of $\int_0^\tau \|\mathbf{u}(s)\|_{L^\infty}^2 ds$. The $L^{\infty,2}$ norm of the maximum velocity is one of the endpoint cases in the the Ladyzhenskaya-Prodi-Serrin regularity criteria with $p = \infty$ and $q = 2$. We observe that this quantity grows almost perfectly linear in τ . This suggests that $\|\mathbf{u}(t)\|_{L^\infty}$ roughly scales like $1/(T - t)^{1/2}$, which provides further evidence for the finite time singularity of the generalized Boussinesq system with constant viscosity.

5.4.3. *The blowup of the negative pressure.* Another blowup criteria is based on the blowup of the negative pressure [71]. In Figure 5.13(a), we plot the minimum of the original pressure p as a function of τ . We observe that the minimum of the pressure approaches to negative infinity. In Figure 5.13(b), we plot the rescaled pressure profile. We observe that the minimum of the rescaled pressure \tilde{p} is negative with its global minimum close to the origin. In Figure 5.14 (a), we plot the dynamic growth of the global minimum of the rescaled pressure \tilde{p} as a function of time. In Figure 5.14 (b), we plot

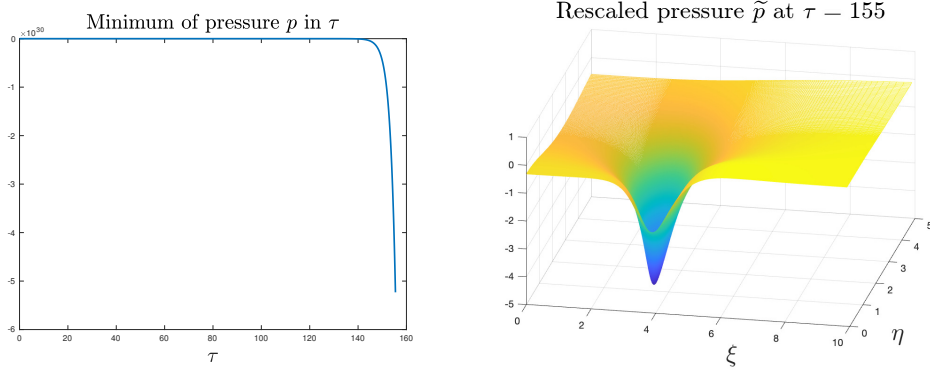


Figure 5.13: Left plot: The minimum of the original pressure p as a function of τ . Right plot: The profile of the rescaled pressure \tilde{p} at $\tau = 155$.

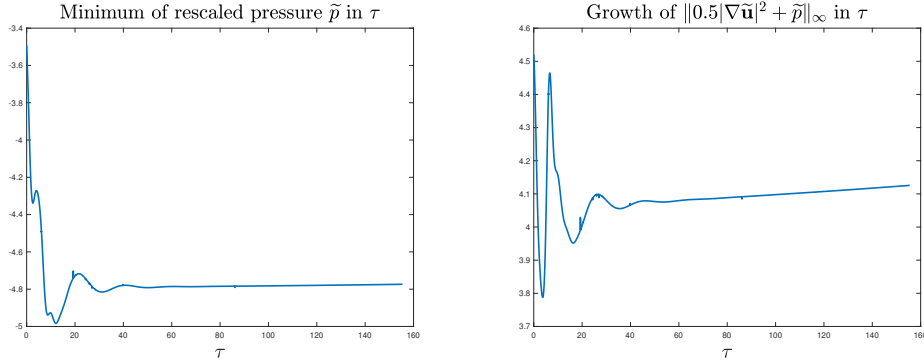


Figure 5.14: Left plot: The minimum of the rescaled pressure \tilde{p} as a function of τ . Right plot: The growth of $\|0.5|\nabla\tilde{\mathbf{u}}|^2 + \tilde{p}\|_\infty$ as a function of τ .

the $\|\frac{1}{2}|\tilde{\mathbf{u}}|^2 + \tilde{p}\|_{L^\infty}$ as a function of time. We can see that both of these two quantities stay bounded and seem to approach to a constant value as $\tau \rightarrow \infty$. Since the original pressure variable p scales like $\|u_1\|_\infty \tilde{p}$, and $\|u_1\|_\infty = 1/(T-t)$, we conclude that the minimum of the pressure goes to minus infinity with a blowup rate $O(1/(T-t))$ as $t \rightarrow T$. Similarly, we conclude that

$$\|p\|_\infty = O\left(\frac{1}{T-t}\right), \quad \left\|\frac{1}{2}|\nabla\mathbf{u}| + p\right\|_\infty = O\left(\frac{1}{T-t}\right).$$

The rapid growth of these two quantities provides additional evidence for the development of potentially singular solutions of the generalized Boussinesq system with constant viscosity [71].

5.4.4. *The growth of the critical L^n norm of the velocity in n dimensions.* We now study the L^n norm of the velocity field. As shown in [30], the 3D Navier–Stokes equations cannot blow up at time T if $\|\mathbf{u}(\tau)\|_{L^3}$ is bounded up to time T . In n dimensions, we should monitor the growth of $\|\mathbf{u}(\tau)\|_{L^n}$, which is scaling invariant. In Figure 5.15 (a), we plot the dynamic growth of $\|\mathbf{u}(\tau)\|_{L^n}$ as a function of time in the late stage. We observe that $\|\mathbf{u}(t)\|_{L^n}$ experiences a mild logarithmic growth. Here we only plot the growth of $\|\mathbf{u}(\tau)\|_{L^n}$ in the late stage.

We remark that the non-blowup criterion for 3D Navier–Stokes using the $\|\mathbf{u}\|_{L^3}$ estimate is based on a compactness argument. As a result, the bound on $\max_{0 \leq t \leq T} \|\mathbf{u}(t)\|_{L^3}$ does not provide a direct estimate on the dynamic growth rate of the 3D Navier–Stokes solution up to T . In a recent paper [76], Tao further examined the role of the L^3 norm of the velocity on the potential blow-up of the 3D Navier–Stokes equations. He showed that as one approaches a finite blow-up time T , the critical L^3

norm of the velocity must blow up at least at a rate $(\log \log \log \frac{1}{T-t})^c$ for some absolute constant c . This implies that even for a potential finite time blow-up of the Navier–Stokes equations, $\|\mathbf{u}(t)\|_{L^3}$ may blow up extremely slowly. Moreover, the blow-up rate could be even slower for higher dimensions. We refer to [67] for a generalized result for dimension $n \geq 4$ by Palasek who showed that $\|\mathbf{u}(t)\|_{L^n}$ must blow up at least at a rate $(\log \log \log \log \frac{1}{T-t})^c$ for some absolute constant c .

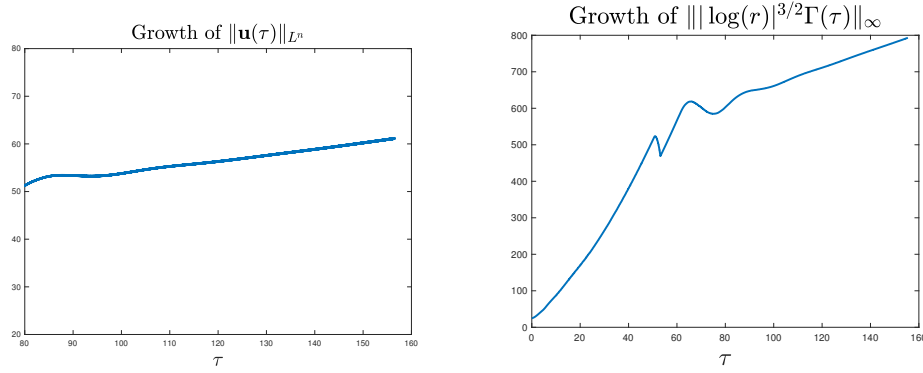


Figure 5.15: Left plot: The dynamic growth of $\|\mathbf{u}(\tau)\|_{L^n}$ as a function of τ . Right plot: The dynamic growth of $\| |\log(r)|^{3/2} \Gamma(\tau, r, z) \|_{L^\infty}$ as a function of τ .

We also examine another non-blowup criteria based on the bound of $\| |\log(r)|^{3/2} \Gamma(t) \|_{L^\infty(r \leq r_0)}$ by D. Wei in [78] (see also a related paper by Lei and Zhang in [55]). In Figure 5.15(b), we plot the dynamic growth of $\| |\log(r)|^{3/2} \Gamma(\tau) \|_{L^\infty(\Omega(\tau))}$ over our expanding computational domain $\Omega(\tau)$. Note that since we only expand the domain by a factor of $Z(t)^{-1/5}$, the actual domain in the original physical space is actually shrinking in time. We observe that this quantity grows roughly linearly in τ in the late stage. This implies that the non-blowup condition stated in [78, 55] is also violated.

Another important non-blowup result is the lower bound on the growth rate of the maximum velocity for the axisymmetric Navier–Stokes equations. The results in [10, 9, 53] imply that the 3D axisymmetric Navier–Stokes equations cannot develop a finite time singularity if the maximum velocity field is bounded by $\|\mathbf{u}(t)\|_{L^\infty} \leq C(T-t)^{1/2}$, provided that $|r\mathbf{u}(t, r, z)|$ remains bounded for $r \geq r_0$ for some $r_0 > 0$. These results are based on some compactness argument. In Figure 5.16, we plot the growth $\|ru^r\|_{L^\infty}$ and $\|ru^z\|_{L^\infty}$ as a function of τ . We observe that $\|ru^r\|_{L^\infty}$ develops a mild linear growth in the late stage of the computation, which violates the non-blowup conditions stated in [10, 9, 53].

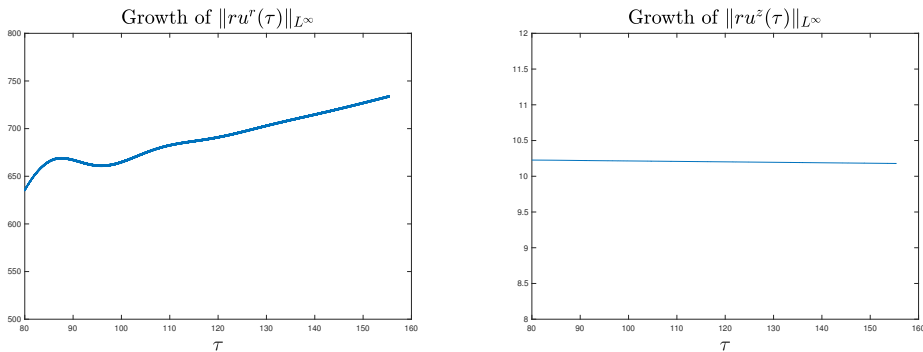


Figure 5.16: Left plot: The dynamic growth of $\|ru^r(\tau)\|_{L^\infty}$ as a function of τ . Right plot: The dynamic growth of $\|ru^z(\tau)\|_{L^\infty}$ as a function of τ .

5.5. Balance between the source term and the diffusion term. In this subsection, we study the balance between the nearly singular Delta function like source term and the diffusion term in the $\tilde{\omega}_1$ equation. Since the density $\tilde{\Gamma}$ satisfies a conservative advection diffusion equation, the nonlinear growth of maximum vorticity is mainly driven by the nearly singular source term in the $\tilde{\omega}_1$ equation. It is important to monitor whether the source term and the diffusion term remain balanced throughout the computation.

In Figure 5.17(a), we plot the ratio between the source term $(\tilde{u}_1^2)_\eta$ and the diffusion term $-\nu_2(\tau)\Delta\tilde{\omega}_1$ at (R_ω, Z_ω) where $\tilde{\omega}_1$ achieves its maximum. Here $\nu_2(\tau) = \nu_2 C_\psi(\tau)/C_{lz}(\tau)$ with $\nu_2 = 0.006$. We observe that the ratio of these two terms has a mild increase in time and settles down to 2.04 at $\tau = 155$. This shows that the vortex stretching term dominates the diffusion throughout the computation. Since the vortex stretching comes from the ω_1 equation only and there is no vortex stretching in the $\tilde{\Gamma}$ equation, the balance between the vortex stretching term and the diffusion term in the $\tilde{\omega}_1$ equation is crucial in maintaining the robust nonlinear growth of the maximum vorticity in time.

Recall that C_{lz} and C_{lr} scale like $\lambda(t)\sqrt{T-t}$. In Figure 5.17(b), we plot the contours of $\tilde{\omega}_1$ as a function of $(\lambda(\tau)(\xi - R_\omega), \lambda(\tau)(\eta - Z_\omega))$ for three different time instants, $\tau = 139, 147, 155$ using resolution 1024×1024 . During this time interval, the maximum vorticity has increased by a factor of 1554. We observe that these contours are almost indistinguishable from each other. This shows that ω_1 actually enjoys a parabolic scaling property within the inner region centered at (R_ω, Z_ω) with local scaling proportional to $C_{lz}/\lambda(t) \sim \sqrt{T-t}$ and $C_{lr}/\lambda(t) \sim \sqrt{T-t}$. This explains why we can achieve the balance between the source term $(\tilde{u}_1^2)_\eta$ and the diffusion term $\nu_2(\tau)\Delta\tilde{\omega}_1$ within this inner region centered at (R_ω, Z_ω) with domain size shrinking to zero at a rate $\lambda(\tau)$.

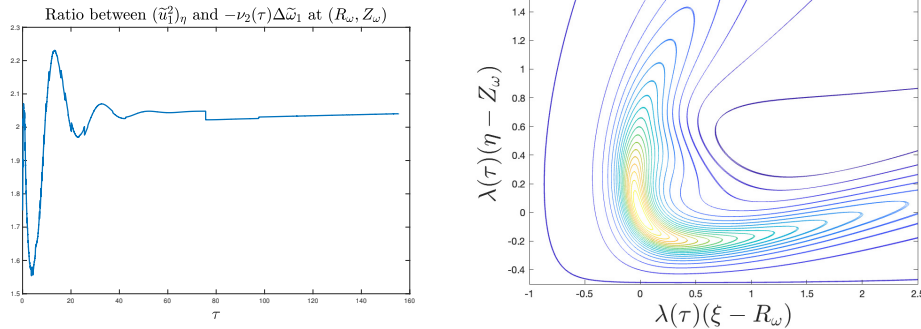


Figure 5.17: Left plot: Ratio between the source term $(\tilde{u}_1^2)_\eta$ and the diffusion term $\nu_2(\tau)\Delta\tilde{\omega}_1$ at (R_ω, Z_ω) as a function of τ , where $\nu_2(\tau) = \nu_2 C_\psi(\tau)/C_{lz}(\tau)$. Right plot: Contours of $\tilde{\omega}_1$ with respect to $((\xi - R_\omega)\lambda(\tau), (\eta - Z_\omega)\lambda(\tau))$ at $\tau = 139, 147, 155$ during which $\|\omega\|_\infty$ has increased by 1554.

6. CONCLUDING REMARKS

In this paper, we presented numerical evidences that the generalized Navier-Stokes equations with solution dependent viscosity and smooth initial data develop a self-similar blowup at the origin in finite time. An important consequence of using this solution dependent viscosity is that the self-similar blowup profile satisfies the self-similar equation for the generalized Navier-Stokes equations with constant viscosity ν_0 . Since the generalized axisymmetric Euler equations enjoy total circulation conservation, we expect that the scaling exponent $\hat{c}_{lr} \rightarrow 1/2$ as $\nu_0 \rightarrow 0$. It would be very interesting if we can solve the self-similar equations directly using some optimization method or PINN [77] with viscosity coefficient ν_0 as a continuation parameter.

We have also investigated the nearly self-similar blowup of the generalized Boussinesq system with two constant viscosity coefficients. The generalized Boussinesq system preserves almost all the known properties of the 3D Navier–Stokes equations with the exception of the angular momentum conservation. To the best of our knowledge, all known blowup criteria can be applied to the generalized Boussinesq system. We have applied several blow-up criteria to study the nearly self-similar blowup of the generalized Boussinesq system with two constant viscosity coefficients, including the L^n norm of the velocity and some non-blowup criteria that are specially derived for the axisymmetric Navier–Stokes equations. All these blowup criteria confirm the potential finite time singularity of the generalized Boussinesq system with constant viscosity.

A novel contribution of this paper is to introduce a two-scale dynamic rescaling formulation. This two-scale formulation enables us to introduce the space dimension as a dynamic variable to eliminate some unstable mode related to the scaling property of the axisymmetric Navier–Stokes equations. We varied the space dimension to ensure that the advection along the r and z directions has the same scaling property, which prevents the development of a two-scale solution structure.

It would be extremely interesting to develop a computer assisted proof to verify the findings obtained in this paper. Since we expect to obtain an asymptotically self-similar blowup for the generalized Navier–Stokes equations with solution dependent viscosity, we may be able to extend the method of analysis developed for the Hou-Luo blowup scenario in [14, 12] to this new blowup scenario.

It would be more challenging to analyze the blowup of the generalized Boussinesq system due to the logarithmic correction. Nearly self-similar blowup with a logarithmic correction has been observed in other nonlinear PDEs. One essential ingredient in the blowup analysis of these nonlinear PDEs is the stability analysis of the linearized operator around the ground state, which is known explicitly. The situation for the incompressible Euler or Navier–Stokes equation is much more complicated since we do not have an explicit ground state and the linearized operator is not compact. We need to develop a new dynamic rescaling formulation that can accommodate nearly self-similar blowup with a logarithmic correction. We have recently made some preliminary progress in extending the method of analysis to analyze the blowup of the semilinear heat equation [42]. We are currently in the process of further extending this technique to more challenging nonlinear PDEs.

Acknowledgments. The research was in part supported by NSF Grant DMS-2205590 and the Choi Family Gift Fund. I would like to thank my student Changhe Yang for a number of stimulating discussions regarding the two-scale dynamic rescaling formulation.

REFERENCES

- [1] J. Beale, T. Kato, and A. Majda. Remarks on the breakdown of smooth solutions for the 3-D Euler equations. *Commun. Math. Phys.*, 94(1):61–66, 1984.
- [2] O. N. Boratav and R. B. Pelz. Direct numerical simulation of transition to turbulence from a high-symmetry initial condition. *Phys. Fluids*, 6:2757–2784, 1994.
- [3] M. Brenner, S. Hormoz, and A. Pumir. Potential singularity mechanism for the Euler equations. *Phys. Rev. Fluids*, 1:084503, 2016.
- [4] T. Buckmaster, S. Shkoller, and V. Vicol. Formation of shocks for 2D isentropic compressible Euler. *Communications on Pure and Applied Mathematics*.
- [5] T. Buckmaster, S. Shkoller, and V. Vicol. Formation of point shocks for 3D compressible Euler. *arXiv preprint arXiv:1912.04429*, 2019.
- [6] L. Caffarelli, R. Kohn, and L. Nirenberg. Partial regularity of suitable weak solutions of the Navier–Stokes equations. *CPAM*, 35(6):771–831, 1982.
- [7] R. E. Caflisch. Singularity formation for complex solutions of the 3D incompressible Euler equations. *Physica D: Nonlinear Phenomena*, 67(1-3):1–18, 1993.

- [8] R. E. Caflisch and O. Orrelana. Singular solutions and ill-posedness for the evolution of vortex sheets. *SIAM J. Appl. Math.*, 20(2):249–510, 1989.
- [9] C. C. Chen, R. M. Strain, T. P. Tsai, and H. T. Yau. Lower bounds on the blow-up rate of the axisymmetric Navier–Stokes equations II. *Commun. PDEs*, 34(3):203–232, 2009.
- [10] C. C. Chen, R. M. Strain, H. T. Yau, and T. P. Tsai. Lower bound on the blow-up rate of the axisymmetric Navier–Stokes equations. *Intern. Math. Res. Notices*, 2008:rnn016, 2008.
- [11] J. Chen. Remarks on the smoothness of the $C^{1,\alpha}$ asymptotically self-similar singularity in the 3D Euler and 2D Boussinesq equations. *arXiv preprint arXiv:2309.00150*, 2023.
- [12] J. Chen and T. Y. Hou. Stable nearly self-similar blowup of the 2D Boussinesq and 3D Euler equations with smooth data II: Rigorous numerics. *arXiv preprint: arXiv:2305.05660 [math.AP]*.
- [13] J. Chen and T. Y. Hou. Finite time blowup of 2D Boussinesq and 3D Euler equations with $C^{1,\alpha}$ velocity and boundary. *CMP*, 383(3):1559–1667, 2021.
- [14] J. Chen and T. Y. Hou. Stable nearly self-similar blowup of the 2D Boussinesq and 3D Euler equations with smooth data I: Analysis. *arXiv preprint: arXiv:2210.07191v3 [math.AP]*, 2022.
- [15] J. Chen, T. Y. Hou, and D. Huang. Asymptotically self-similar blowup of the Hou-Luo model for the 3D Euler equations. *arXiv:2106.05422 [math.AP]*, 2021.
- [16] J. Chen, T. Y. Hou, and D. Huang. On the finite time blowup of the De Gregorio model for the 3D Euler equation. *CPAM*, <https://doi.org/10.1002/cpa.21991>, 2021.
- [17] A. Cheskidov. Blow-up in finite time for the dyadic model of the Navier–Stokes equations. *AMS Tran.*, 360:5101–5120, 2008.
- [18] K. Choi, T. Y. Hou, A. Kiselev, G. Luo, V. Sverak, and Y. Yao. On the finite-time blowup of a 1D model for the 3D axisymmetric Euler equations. *CPAM*, 70(11):2218–2243, 2017.
- [19] K. Choi, A. Kiselev, , and Y. Yao. Finite time blow up for a 1D model of 2D Boussinesq system. *CMP*, 334(3):1667–1679, 2015.
- [20] P. Constantin, C. Fefferman, and A. Majda. Geometric constraints on potentially singular solutions for the 3-D Euler equations. *Commun. PDEs*, 21:559–571, 1996.
- [21] D. Córdoba and L. Martínez-Zorúa. Blow-up for the incompressible 3d-euler equations with uniform $C^{1,1/2-\epsilon} \cap L^2$ force. *arXiv preprint arXiv:2309.08495*, 2023.
- [22] D. Cordoba, L. Martinez-Zorúa, and F. Zheng. Finite time singularities to the 3D incompressible Euler equations for solutions in $C^{1,\alpha} \cap C^\infty(\mathbb{R}^3 \setminus \{0\}) \cap L^2$. *arXiv preprint arXiv:2308.12197*, 2023.
- [23] J. Deng, T. Y. Hou, and X. Yu. Geometric properties and non-blowup of 3D incompressible Euler flow. *Commun. PDEs*, 30:225–243, 2005.
- [24] T. D. Drivas and T. Elgindi. Singularity formation in the incompressible Euler equation in finite and infinite time. *EMS Surveys in Mathematical Sciences*, 10(1):1–100, 2023.
- [25] W. E and C.-W. Shu. Small-scale structures in Boussinesq convection. *Phys. Fluids*, 6:49–58, 1994.
- [26] T. M. Elgindi. Finite-time singularity formation for $C^{1,\alpha}$ solutions to the incompressible euler equations on \mathbb{R}^3 . *Annals of Mathematics*, 194(3):647–727, 2021.
- [27] T. M. Elgindi, T. Ghou, and N. Masmoudi. On the stability of self-similar blow-up for $C^{1,\alpha}$ solutions to the incompressible Euler equations on R^3 . *arXiv:1910.14071*, 2019.
- [28] T. M. Elgindi and F. Pasqualotto. From instability to singularity formation in incompressible fluids. *arXiv preprint arXiv:2310.19780*, 2023.
- [29] T. M. Elgindi and F. Pasqualotto. Invertibility of a linearized boussinesq flow: a symbolic approach. *arXiv preprint arXiv:2310.19781*, 2023.
- [30] L. Escauriaza, G. Seregin, and V. Sverak. $L_{3,\infty}$ -solutions to the Navier–Stokes equations and backward uniqueness. *Russian Mathematical Surveys.*, 58(2):211–250, 2003.
- [31] C. Fefferman. Existence and smoothness of the Navier–Stokes equation. *The millennium prize problems*, pages 57–67, 2006.

- [32] J. Gibbon. The three-dimensional Euler equations: Where do we stand? *Physica D*, 237:1894–1904, 2008.
- [33] R. Grauer and T. C. Sideris. Numerical computation of 3D incompressible ideal fluids with swirl. *Phys. Rev. Lett.*, 67:3511–3514, 1991.
- [34] E. Hopf. über die anfangswertaufgabe für die hydrodynamischen grundgleichungen. *Math. Nachr.*, 4:213–231, 1951.
- [35] T. Y. Hou. Potential singularity of the 3D Euler equations in the interior domain. *Found Comput Math*, 23:2203–2249, 2023.
- [36] T. Y. Hou. The potentially singular behavior of the 3D Navier–Stokes equations. *Found Comput Math*, 23:2251–2299, 2023.
- [37] T. Y. Hou and D. Huang. A potential two-scale traveling wave asingularity for 3D incompressible Euler equations. *Physica D*, 435:133257, 2022.
- [38] T. Y. Hou and D. Huang. Potential singularity formation of 3D axisymmetric Euler equations with degenerate viscosity coefficients. *MMS*, 21(1):218–268, 2023.
- [39] T. Y. Hou and C. Li. Dynamic stability of the three-dimensional axisymmetric Navier–Stokes equations with swirl. *CPAM*, 61(5):661–697, 2008.
- [40] T. Y. Hou and R. Li. Dynamic depletion of vortex stretching and non-blowup of the 3-D incompressible Euler equations. *J. Nonlinear Sci.*, 16:639–664, 2006.
- [41] T. Y. Hou and R. Li. Blowup or no blowup? the interplay between theory and numerics. *Physica D.*, 237:1937–1944, 2008.
- [42] T. Y. Hou, V. T. Nguyen, and Y. Wang. L2-based stability of blowup with log correction for semilinear heat equation. *arXiv preprint: arXiv:2404.09410v1 [math.AP]*, 2024.
- [43] T. Y. Hou and S. Zhang. Potential singularity of the axisymmetric Euler equations with C^α initial vorticity for a large range of α . Part I. the 3-dimensional case. *arXiv preprint: arXiv:2212.11912 [math.AP]*, 2022.
- [44] T. Y. Hou and S. Zhang. Potential singularity of the axisymmetric Euler equations with C^α initial vorticity for a large range of α . Part II. the n -dimensional case. *arXiv preprint: arXiv:2212.11924 [math.AP]*, 2022.
- [45] D. Huang, X. Qin, X. Wang, and D. Wei. On the exact self-similar finite-time blowup of the Hou-Luo model with smooth profiles. *arXiv preprint: arXiv:2308.01528v1 [math.AP]*, 2023.
- [46] D. Huang, X. Qin, X. Wang, and D. Wei. Self-similar finite-time blowups with smooth profiles of the generalized Constantin-Lax-Majda model. *arXiv preprint: arXiv:2305.05895 [math.AP]*, 2023.
- [47] C. E. Kenig and F. Merle. Global well-posedness, scattering and blow-up for the energy-critical, focusing, non-linear Schrödinger equation in the radial case. *Inventiones mathematicae*, 166(3):645–675, 2006.
- [48] R. M. Kerr. Evidence for a singularity of the three-dimensional incompressible Euler equations. *Phys. Fluids A*, 5:1725–1746, 1993.
- [49] A. Kiselev. Small scales and singularity formation in fluid dynamics. In *Proceedings of the International Congress of Mathematicians*, volume 3, 2018.
- [50] A. Kiselev and O. Ladyzhenskaya. On the existence and uniqueness of the solution of the nonstationary problem for a viscous, incompressible fluid. *Izv. Akad. Nauk SSSR. Ser Mat.*, 21(5):655–690, 1957.
- [51] A. Kiselev, L. Ryzhik, Y. Yao, and A. Zlatos. Finite time singularity for the modified SQG patch equation. *Ann. Math.*, 184:909–948, 2016.
- [52] A. Kiselev and V. Sverak. Small scale creation for solutions of the incompressible two dimensional Euler equation. *Annals of Mathematics*, 180:1205–1220, 2014.
- [53] G. Koch, N. Nadirashvili, G. Seregin, and V. Sverak. Liouville theorems for the Navier–Stokes equations and applications. *Acta Mathematica*, 203(1):83–105, 2009.

- [54] M. J. Landman, G. C. Papanicolaou, C. Sulem, and P.-L. Sulem. Rate of blowup for solutions of the nonlinear Schrödinger equation at critical dimension. *Phys. Rev. A* (3), 38(8):3837–3843, 1988.
- [55] Z. Lei and Q. Zhang. Criticality of the axially symmetric Navier–Stokes equations. *Pacific Journal of Mathematics*, 289(1):169–187, 2017.
- [56] J. Leray. Sur le mouvement d’un liquide visqueux emplissant l’espace. *Acta Math.*, 63(1):193–248, 1934.
- [57] F. Lin. A new proof of the Caffarelli–Kohn–Nirenberg theorem. *CPAM*, 51(3):241–257, 1998.
- [58] J. Liu and W. Wang. Convergence analysis of the energy and helicity preserving scheme for axisymmetric flows. *SINUM*, 44(6):2456–2480, 2006.
- [59] G. Luo and T. Y. Hou. Potentially singular solutions of the 3D axisymmetric Euler equations. *Proceedings of the National Academy of Sciences*, 111(36):12968–12973, 2014.
- [60] G. Luo and T. Y. Hou. Toward the finite-time blowup of the 3D axisymmetric Euler equations: a numerical investigation. *Multiscale Modeling & Simulation*, 12(4):1722–1776, 2014.
- [61] A. Majda and A. Bertozzi. *Vorticity and incompressible flow*, volume 27. Cambridge University Press, 2002.
- [62] Y. Martel, F. Merle, and P. Raphaël. Blow up for the critical generalized Korteweg–de Vries equation. I: Dynamics near the soliton. *Acta Mathematica*, 212(1):59–140, 2014.
- [63] D. McLaughlin, G. Papanicolaou, C. Sulem, and P. Sulem. Focusing singularity of the cubic schrödinger equation. *Physical Review A*, 34(2):1200, 1986.
- [64] F. Merle and P. Raphael. The blow-up dynamic and upper bound on the blow-up rate for critical nonlinear Schrödinger equation. *Annals of mathematics*, 161:157–222, 2005.
- [65] F. Merle and H. Zaag. Stability of the blow-up profile for equations of the type $u_t = \Delta u + |u|^{p-1}u$. *Duke Math. J.*, 86(1):143–195, 1997.
- [66] F. Merle and H. Zaag. On the stability of the notion of non-characteristic point and blow-up profile for semilinear wave equations. *Communications in Mathematical Physics*, 333(3):1529–1562, 2015.
- [67] S. Palasek. A minimum critical blowup rate for the high-dimensional Navier–Stokes equations. *Journal of Mathematical Fluid Mechanics*, 24(4):1–28, 2022.
- [68] W. Pauls, T. Matsumoto, U. Frisch, and B. J. Nature of complex singularities for the 2D Euler equation. *Physica D: Nonlinear Phenomena*, 219(1):40–59, 2006.
- [69] G. Prodi. Un teorema di unicità per le equazioni di Navier–Stokes. *Ann. Math. Pura Appl.*, 4(48):173–182, 1959.
- [70] B. Protas. Systematic search for extreme and singular behaviour in some fundamental models of fluid mechanics. *Philosophical Transactions A*, 380:20210035, 2022.
- [71] G. Seregin and V. Sverak. Navier–Stokes equations with lower bounds on the pressure. *Arch. Rat. Mech. Anal.*, 9(1):65–86, 2002.
- [72] J. Serrin. On the interior regularity of weak solutions of the Navier–Stokes equations. *Arch. Ration. Mech. Anal.*, 9:187–191, 1962.
- [73] M. Siegel and R. E. Caflisch. Calculation of complex singular solutions to the 3D incompressible Euler equations. *Physica D: Nonlinear Phenomena*, 238(23):2368–2379, 2009.
- [74] A. Soffer and M. I. Weinstein. Multichannel nonlinear scattering for nonintegrable equations. *Comm. Math. Phys.*, 133:119–146, 1990.
- [75] T. Tao. Finite time blowup for an averaged three-dimensional Navier–Stokes equation. *J. Amer. Math. Soc.*, 29:601–674, 2016.
- [76] T. Tao. Quantitative bounds for critically bounded solutions to the Navier–Stokes equations. *arXiv:1908.04958v2 [math.AP]*, 2020.
- [77] Y. Wang, C. Y. Lai, J. Gomez-Serrano, and T. Buckmaster. Asymptotic self-similar blow-up profile for three-dimensional axisymmetric Euler equations using neural networks. *Phys. Rev. Lett.*, 130:244002, 2023.

- [78] D. Wei. Regularity criterion to the axially symmetric Navier–Stokes equations. *J. Math. Anal. Appl.*, 435(1):402–413, 2016.

APPLIED AND COMPUTATIONAL MATHEMATICS, CALIFORNIA INSTITUTE OF TECHNOLOGY, PASADENA, CA 91125, USA
Email address: hou@cms.caltech.edu